

Circulation on the central Bering Sea shelf, July 2008 to July 2010

S. Danielson,¹ T. Weingartner,¹ K. Aagaard,² J. Zhang,² and R. Woodgate²

Received 21 June 2012; revised 27 July 2012; accepted 17 August 2012; published 3 October 2012.

[1] We examine the July 2008 to July 2010 circulation over the central Bering Sea shelf using measurements at eight instrumented moorings, hindcast winds and numerical model results. At sub-tidal time scales, the vertically integrated equations of motion show that the cross-shelf balance is primarily geostrophic. The along-shelf balance is also mainly geostrophic, but local accelerations, wind stress and bottom friction account for 10–40% of the momentum balance, depending on season and water depth. The shelf exhibits highly variable flow with small water column average vector mean speeds ($<5 \text{ cm s}^{-1}$). Mean/peak speeds in summer ($3\text{--}6 \text{ cm s}^{-1}/10\text{--}30 \text{ cm s}^{-1}$) are smaller than in winter and fall ($6\text{--}12 \text{ cm s}^{-1}/30\text{--}70 \text{ cm s}^{-1}$). Low frequency flows ($<1/4$ cpd) are horizontally coherent over distances exceeding 200 km. Vertical coherence varies seasonally, degrading with the onset of summer stratification. Because effects of heating and freezing are enhanced in shallow waters, warm summers increase the cross-shelf density gradient and thus enhance northward transport; cold winters with increased ice production and brine rejection increase the (now reversed) cross-shelf density gradient and enhance southward transport. Although the baroclinic velocity is large enough to influence seasonal transports, wind-forced Ekman dynamics are primarily responsible for flow variations. The system changes from strong northward flow (with coastal convergence) to strong southward flow (with coastal divergence) for northerly and easterly winds, respectively. Under northerly and northwesterly winds, nutrient-rich waters flow toward the central shelf from the north and northwest, replacing dilute coastal waters that are carried south and west.

Citation: Danielson, S., T. Weingartner, K. Aagaard, J. Zhang, and R. Woodgate (2012), Circulation on the central Bering Sea shelf, July 2008 to July 2010, *J. Geophys. Res.*, 117, C10003, doi:10.1029/2012JC008303.

1. Introduction

[2] The shallow and broad central Bering Sea shelf is the region south of St. Lawrence Island and north of Nunivak Island (Figure 1). It experiences cooling, ice formation and brine production in winter [Drucker *et al.*, 2003], solar heating in summer, strong winds in fall, winter and early spring [Brower *et al.*, 1988; Bond *et al.*, 1994], large river discharges in summer [Brabets *et al.*, 2000], and strong tidal currents [Pearson *et al.*, 1981; Moffeld, 1984; Kowalik, 1999; Danielson and Kowalik, 2005]. Thermohaline characteristics exhibit large inter-annual variability [Takenouti and Ohtani, 1974; Coachman *et al.*, 1975; Danielson *et al.*, 2011], but the causes of these variations are not fully understood.

[3] North of St. Lawrence Island, the shelf flow is dominated by a net northward transport through Bering Strait of $\sim 0.8 \text{ Sv}$ ($1 \text{ Sv} = 10^6 \text{ m}^3 \text{ s}^{-1}$) [Roach *et al.*, 1995; Woodgate *et al.*, 2005a], ascribed to a sea surface height difference of $\sim 0.5 \text{ m}$ between the North Pacific and Arctic oceans [Stigebrandt, 1984; Overland and Roach, 1987; Aagaard *et al.*, 2006; Woodgate *et al.*, 2005b], and in opposition to the mean wind. Westward intensification associated with the topographic beta effect forces Bering Sea slope waters on-shelf through the Gulf of Anadyr [Kinder *et al.*, 1986; Danielson *et al.*, 2012]. Measurements [Muench *et al.*, 1988; Coachman, 1993] and models [Overland and Roach, 1987; Spaulding *et al.*, 1987; Clement *et al.*, 2005] suggest that 70–80% of the Bering Strait flow first passes through Anadyr Strait, with the rest flowing through Shpanberg Strait. Mooring- and satellite-based estimates of the instantaneous transport through Bering Strait range between about -3 Sv to $+4 \text{ Sv}$ [Coachman and Aagaard, 1988; Roach *et al.*, 1995; Cherniawsky *et al.*, 2005; Woodgate *et al.*, 2005a]. Numerical model results and observations [Overland and Roach, 1987; Muench *et al.*, 1988; Danielson *et al.*, 2012] indicate that flows in Shpanberg Strait can reverse to southward while the flow in Anadyr Strait is northward. Mean northerly winter winds (blowing toward the south) retard the northward transport in Bering Strait [Overland and Roach, 1987], so that October–March northward transports

¹Institute of Marine Science, School of Fisheries and Ocean Science, University of Alaska Fairbanks, Fairbanks, Alaska, USA.

²Polar Science Center, Applied Physics Laboratory, University of Washington, Seattle, Washington, USA.

Corresponding author: S. Danielson, Institute of Marine Science, School of Fisheries and Ocean Science, O'Neill Building, Rm. 114, University of Alaska Fairbanks, Fairbanks, AK 99775-7220, USA. (seth@ims.uaf.edu)

©2012. American Geophysical Union. All Rights Reserved.
10.1029/2012JC008303

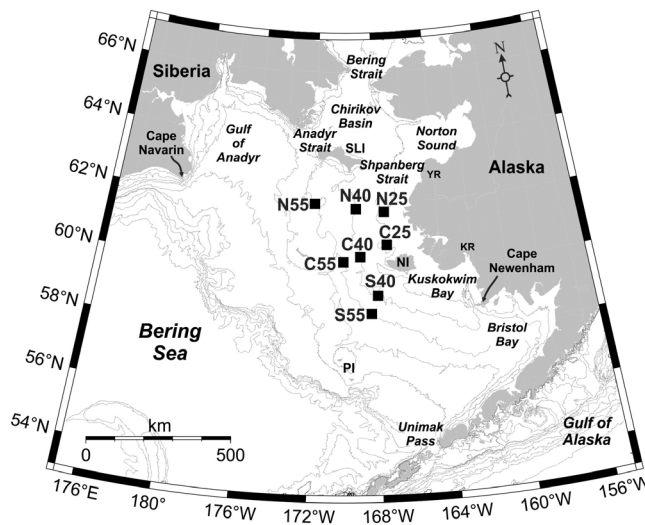


Figure 1. The eastern Bering Sea with place names and mooring sites (squares). SLI = St. Lawrence Island, NI = Nunivak Island, PI = Pribilof Islands. River names YR = Yukon River and KR = Kuskokwim River are placed near the river mouths. Bathymetric contours are for 25 m, 40 m, 55 m, 70 m, 100 m, 200 m, 500 m, 1000 m, 2000 m, 3000 m, 4000 m, and 5000 m.

are typically one-half to two-thirds those of April–August [Roach et al., 1995; Woodgate et al., 2005a].

[4] Over the inner (0–50 m depths) and middle (50–100 m depths) southeastern Bering shelf, tidal currents are large (the two largest tidal constituents, M_2 and K_1 , sum to 25–55 cm s^{-1}) [Pearson et al., 1981; Kowalik, 1999; Stabeno et al., 2010], and mean subtidal flows are small (1–5 cm s^{-1}) [Schumacher and Kinder, 1983; Stabeno et al., 2010]. The middle shelf contains cold waters below the summer pycnocline [Coachman, 1986]. The southern extent of this “cold pool” is primarily determined by the previous winter’s ice extent [Stabeno et al., 2001; Zhang et al., 2012]. Currents over the outer shelf (between the shelfbreak and 100 m isobath) are 1–10 cm s^{-1} , with the flow more or less steadily northward along the isobaths [Kinder and Schumacher, 1981; Schumacher and Kinder, 1983; Schumacher and Reed, 1992; Stabeno et al., 2001; Stabeno et al., 2002a]. Along the continental slope, the Bering Slope Current is a relatively swift (5–20 cm s^{-1}), deep, and strongly eddying cyclonic boundary current with a transport of ~ 6 Sv [Favorite, 1974; Royer and Emery, 1984; Okkonen, 1993; Overland et al., 1994; Roden, 1995; Johnson et al., 2004; Clement Kinney et al., 2009; Stabeno et al., 2009]. Inflow from the Gulf of Alaska through Unimak Pass [Schumacher et al., 1982; Stabeno et al., 2002b] delivers low-salinity waters from the Gulf of Alaska, representing a first-order contribution to the shelf fresh water budget [Weingartner et al., 2005; Aagaard et al., 2006].

[5] Inter-annual temperature variations over the southeastern shelf in spring are related to the previous winter’s sea ice extent and timing of retreat [Stabeno et al., 2001; Stabeno et al., 2002b]. Ice extent, in turn, is related to the combination of southward advection of ice caused by northerly wind and low air temperatures [Overland and Pease, 1982; Niebauer et al., 1999]. At the end of summer, heat content over the central and southeastern shelf reflects a combination of the

heating season’s incoming solar radiation and along-shelf transport anomalies, whereas the fresh water content appears to be set by the previous winter’s cross-shelf transport anomaly in conjunction with river discharge, ice melt, precipitation, and evaporation [Danielson et al., 2011].

[6] The central shelf is understudied compared to the southeastern shelf and Bering Strait. The Yukon River (sixth-largest in North America), discharges adjacent to the central shelf, nearly 90% of its annual discharge ($\sim 200 \text{ km}^3$) occurring between May and October [Brabets et al., 2000]. A mean eastward flow south of St. Lawrence Island (mostly confined to within ~ 70 km of the coast [Danielson et al., 2006]) turns northward in Shpanberg Strait, where it encounters the Yukon plume. This eastward flow can reverse under strong northerly and easterly winds [Schumacher et al., 1983; Danielson et al., 2006]. There are relatively few measurements south of this eastward flow and north of St. Matthew and Nunivak islands, but the available data suggest highly variable flows with a net northward drift [Kinder and Schumacher, 1981; Aagaard and Schumacher, 1985; Muench et al., 1988; Danielson et al., 2006].

[7] Winter ice formation and southward ice drift depend on favorable winds [Muench and Ahlmas, 1976; Pease, 1980; McNutt, 1981]. Northerly winds promote southward transport of dilute waters [Zhang et al., 2010] produced by melting along the southern edge of the ice pack [Pease, 1981]. These winds also promote ice formation and dense water formation over the northern shelf. Brine generated by ice formation in polynyas results in density gradients capable of driving a baroclinic pressure gradient large enough to be important to the momentum balance [Schumacher et al., 1983].

[8] Density gradients along the Alaskan coast during summer impel a northward buoyancy-driven coastal jet [Danielson et al., 2011]. The front, which traps river discharge close to the coast through the summer months, likely breaks down in fall with the onset of strong wind-forcing. Danielson et al. [2006] observed that near-surface (1 m and 10 m drogued depths) satellite-tracked drifters exhibited westward motion in the fall and suggested that this motion occurs annually.

[9] Our primary goal here is to gain a better mechanistic understanding of the central shelf flow and its relation to the varying wind and thermohaline fields. Our results bear on numerous eco- and climate system issues, including aspects of salmon migratory behavior [Mundy and Evenson, 2011], advection of passively drifting larvae [Wespestad et al., 2000; Wilderbuer et al., 2002; Orensanz et al., 2004], nutrient replenishment and net production over the Bering shelf [Sambrotto et al., 1986; Whitedge et al., 1986; Mathis et al., 2010], and heat, nutrient, and fresh water fluxes northward into the Arctic Ocean [Aagaard and Carmack, 1989; Woodgate et al., 2010].

[10] We begin with a descriptive overview of the oceanic and atmospheric conditions during the field program, and a kinematic summary of the flow field. We then investigate the circulation dynamics by examining the vertically integrated equations of motion, along with geostrophic velocity computations. Finally, we use model-based sea surface height (SSH) hindcasts and analyses of the vertical and horizontal structure of the flow field to investigate the effects of variable wind-forcing, with particular emphasis on the wind direction. These results are a companion to and provide detailed context

for the bi-modal Bering shelf circulation scheme recently proposed by *Danielson et al.* [2012].

[11] The results described here are part of the National Science Foundation's Bering Ecosystem Study (NSF-BEST) program, the North Pacific Research Board's Bering Sea Integrated Ecosystem Research Program (NPRB-BSIERP) (Program summary 2010, http://doc.nprb.org/web/BSIERP/zzWebsite/proj_mgmt/01.10_bsag_web.pdf) and the National Oceanic and Atmospheric Administration's Bering-Aleutian Salmon International Survey (NOAA-BASIS) program. Collectively, these programs supported an intensive set of collaborative field surveys, modeling efforts and analyses between 2007 and 2011. Our primary data set here is from eight moorings on the central Bering shelf, deployed during July 2008–July 2010 as part of the NSF-BEST program.

[12] Data sets, data calibration and quality control, and numerical model fields are described in section 2. Section 3 presents results in three major subsections: an overview of the current meter, temperature, salinity and wind records (sections 3.1–3.3); the vertically integrated momentum balance and an evaluation of baroclinic contributions (section 3.4); and an analysis of co-variability of the current, wind and sea surface height (SSH) fields (section 3.5). A discussion of the results and a summary are given in sections 4 and 5, respectively.

2. Data and Methods

2.1. Mooring Configurations

[13] From July 2008 to July 2010, eight subsurface moorings were deployed on the 55 m, 40 m and 25 m isobaths (Figure 1 and Table 1) for one year at a time. Moorings on the 40 m and 55 m isobaths were each equipped with an upward-looking Teledyne RDI acoustic Doppler current profiler (ADCP) mounted just above the acoustic release. A Seabird (SBE) temperature/conductivity (T/C) data logger was co-located with the acoustic release; a second SBE T/C data logger was at ~20 m depth. Some of the T/C loggers also recorded pressure (P). Moorings on the 55 m isobath each had a T/C/P data logger at 10 m, connected to the rest of the mooring via a weak link, and an inductive modem transmitted the data to a remote data logger mounted near the 20 m T/C recorder. This configuration permitted measurements close to the surface while providing some protection to the data and the mooring in the event that ice keels or extreme waves destroyed or removed the uppermost float. The configuration worked well. Although we lost four of the six 10 m instruments, we obtained data through the breakdown of fall stratification in both years. Also mounted on the 55 m moorings was a string of thermistors spaced 2–4 m apart between the 20 m and near-bottom T/C recorders.

[14] Moorings on the 25 m isobath employed Oceanscience Group SeaSpider tripod frames. Each was equipped with a gimbaled upward-looking ADCP and T/C/P recorder with pumped intake about 1 m above the seafloor. On the 2009 recovery attempt, one 25 m tripod deployed just south of Nunivak Island was located acoustically, but never recovered. Based on visual inspection by divers we believe that the entire tripod was buried by sediment. As a consequence we did not re-deploy at this site in the second field year. The 2008–2009 N25 tripod popup buoy canister was also fouled by bottom

sediment and unrecoverable from the surface, but we were able to recover it with the aid of divers in the summer of 2010.

[15] In the mooring names, the first letter indicates relative latitudinal positioning within our mooring array (N = north, C = central, S = south) and the subsequent numbers (55, 40, 25) indicate approximate water depth.

2.2. Moored Velocity Data

[16] With the exception of C55 (whose batteries died prematurely in late May 2009 and late February 2010), nearly two complete years of current measurements were recorded at all mooring sites. Velocity data were recorded with 307 KHz Teledyne RDI ADCPs using 30-min ensembles and 1 m bins at 175 pings per ensemble. This protocol yields an expected standard deviation of 1 cm/s for each ensemble. Data within 6% of the distance from the surface to the transducer are affected by sidelobe contamination and discarded. Data were screened with the following thresholds: correlation limit of 64 counts, error amplitude limit of 80 mm/s, and minimum of 40 percent-good pings within any ensemble. Both 3-beam and 4-beam solutions that achieved these criteria were retained. Velocity vector directions were corrected for magnetic declination based on the declination computed halfway through each deployment at each mooring site (corrections ranged from 8.9° to 11.3°).

[17] Velocity data were de-tided using the MATLAB T_Tide [*Pawlowicz et al.*, 2002] harmonic analysis algorithm following *Foreman* [1978] or through low-pass filtering. Filters to isolate sub-tidal (>35 h) and long period (>100 h) currents were implemented with a 6th order bi-directional Butterworth filter. Subtracting both the harmonic tide prediction and the 35-h low-pass signal from the original time series allows us to isolate non-tidal high frequency fluctuations (e.g., inertial motions).

[18] Error estimates for the velocity components are based on estimates of the integral time scale, following *Allen and Kundu* [1978], *Schumacher and Kinder* [1983], and *Emory and Thompson* [2001]. Such computations are noisy in practice but analyses of the 35 h low-pass filtered velocity records at all mooring sites suggest a decorrelation time scale less than 48 h (87% of the estimates gave a time scale shorter than this). As a conservative estimate, therefore, we use 48 h to define the effective degrees of freedom.

2.3. Moored Pressure, Temperature and Salinity Data

[19] Each mooring hosted an assortment of T, T/C and T/C/P data loggers (Table 1). Seabird SBE-16 and SBE-37 instruments were calibrated at the manufacturer's facility prior to deployment and after recovery. Exceptions were the 2009–2010 N55 20 m depth instrument, which failed beyond repair, and some of the 10 m SBE-37 instruments, which were lost during the course of the winter. The magnitude of the temperature drift of the SBEs was less than 0.001°C over the course of one year. Conductivity cell drift resulted in salinity changes from –0.003 to –0.064 (measured at 3.0 S/m) with the exception of the 20 m instrument on C40, which drifted by –0.154. Inspection of the salinity time series suggests that the calibrations did not capture some drift or transient offsets. For example, by late spring of the first year, the near-bottom data logger on two of the moorings showed water less dense than at 20 m. This likely resulted from biofouling or silting of the near-bottom conductivity cell over the course of the winter,

Table 1. Mooring Deployment Details^a

Mooring	Deployment Dates	Latitude (°N)	Longitude (°W)	Bottom Depth (m)	ADCP Depth (m)	SBE16 Depth (m)	SBE37 Depth (m)	HOBO Depth (m)
N55	7/12/2008–7/15/2009	61.9620	–171.9700	54.4	49.4	19.4	52.2, 9.6	23.4, 25.9, 28.4, 30.9, 33.4, 35.9, 38.4, 40.9, 43.4, 45.9, 48.4
C55	7/12/2008–7/11/2009	60.1730	–170.0900	55	47	22	52, 10	23.6, 25.6, 26.8, 28.4, 30, 31.6, 33.2, 34.8, 36.4, 38, 39.6, 41.2, 42.8, 44.4, 46
S55	7/15/2008–7/9/2009	58.5900	–168.3900	55	47	22	52, 10	14, 17, 25.3, 26.8, 28.4, 30, 31.6, 33.2, 36.4, 38, 29.6, 41.2, 42.8, 44.4, 46
N40	7/13/2008–7/14/2009	61.8050	–169.2800	41.7	36.7	20	37.7	
C40	7/10/2008–7/11/2009	60.3390	–169.0200	40.5	35.5	20	36.5	
S40	7/7/2008–7/10/2009	59.1370	–167.9800	41.5	36.5	20	37.5	
N25	7/13/2008–7/25/2010 ^b	61.7000	–167.4500	25.6	24.8	24.6		
C25	7/10/2008–7/11/2009	60.6830	–167.3400	26	25.2	25		
N55	7/15/2009–7/28/2010	61.9690	–171.9800	54.2	49.2	17.1	50.0, 10.9	22, 24, 26, 28, 30, 32, 34, 48
C55	7/11/2009–7/27/2010	60.1730	–170.0900	56	47	20.7	51, 9.8	23.6, 25.2, 26.8, 28.4, 30, 31.6, 33.2, 34.8, 36.4, 38, 39.6, 41.2, 42.8, 44.4, 46
S55	7/9/2009–7/23/2010	58.5900	–168.3900	55.6	47	20.2	51, 10.2	14, 17, 23.6, 25.2, 26.8, 28.4, 30, 31.6, 33.2, 34.8, 36.4, 38, 39.6, 41.2, 42.8, 46
N40	7/14/2009–7/26/2010	61.8080	–169.2800	42	37	20	38	
C40	7/12/2009–7/26/2010	60.3380	–169.0200	40.6	35.6	20	36.6	
S40	7/10/2009–7/23/2010	59.1340	–167.9800	41.5	36.5	20	37.5	
N25	7/16/2009–7/25/2010	61.6910	–167.4200	24	23.2	23		
C25	7/11/2009–7/24/2010	60.6830	–167.3400	26	25.2	25		

^aColumns denote the name, date, location and instrument depths (m). Mooring names beginning with N, C or S, signify the northern, central and southern array lines, respectively. The numbers 55, 40 or 25 denote the nominal water column depth at each deployment site. ADCP records for N40 in 2010 and C55 and S55 in both years ended early due to premature battery failure (see Figure 4 for actual duration of ADCP data coverage).

^bMooring N25 was not recovered in 2009 due to a fouled recovery line canister, but divers recovered it in 2010.

sediment that was not retained in the cell prior to the factory post-season calibration. In any case, we were unable to correct these measurements for such fouling and present herein only the salinity measurements from near 20 m depth. All

salinity data (moored and CTD) are based on the Practical Salinity Scale 1978 [U.N. Educational, Scientific and Cultural Organization, 1981].

[20] Onset HOBO Water Temp Pro v2 temperature loggers were mounted on the 55 m moorings in order to increase vertical resolution (Table 1) of temperature measurements. The HOBO loggers are accurate to within 0.2°C , with a resolution of 0.02°C . Mean temperature differences in February between the upper (20 m and 10 m SBE-37 s) and lower (~ 45 m) Seabird instruments on the 55 m moorings is less than 0.01°C . Therefore, the water column is nearly thermally homogeneous in February and we are able to compute offsets for each HOBO logger based on the average of the temperatures measured by the Seabird temperature probes. HOBO logger offset corrections range between -0.11°C and $+0.06^{\circ}\text{C}$. We have no means to assess HOBO thermistor temperature-dependent bias or drift over the course of the deployment.

2.4. Shipboard Temperature and Salinity Data

[21] The BEST, BSIERP and BASIS programs sponsored 21 oceanographic cruises that sampled in the study region between March and mid-October over the five-year interval 2006–2010. Data from 14 of these cruises falls within two seasonal intervals relevant to our analysis: March to early June and August to October. Moored observations made between 1995 and 2011 (an interval with near-continual in situ monitoring by moored sensors at NOAA station M2 in the southeast Bering Sea) show that the 2007–2010 cruises took place following relatively cold winters, while the 2005–2006 winter was close to average [Stabeno *et al.*, 2012]. Profiles collected by SBE-911 CTD instruments on these cruises are used to provide an overview of the seasonal changes in salinity stratification and to estimate geopotential height anomalies and geostrophic velocities associated with the in situ density structure. Processing techniques varied slightly among responsible institutions, but in each case we employ the final 1 db bin-averaged data set. We estimate that temperatures are generally accurate to within 0.01°C and salinity to within 0.02.

2.5. Gridded Sea Surface Temperatures and Ice Concentrations

[22] To supplement the moored temperature time series, we employ the Reynolds Optimum Interpolation Sea Surface Temperature (OISST) product, version OI.v2 [Reynolds and Smith, 1994; Reynolds *et al.*, 2002], which is generated daily on a $1/4^{\circ}$ grid and incorporates in situ (ship, buoy and drifter) observations along with satellite observations and simulated SST estimates in regions with sea ice [Reynolds *et al.*, 2002]. Satellite-based estimates of sea ice concentration are also included in the OI.v2 data set. Comparing the OI.v2 surface temperatures to temperatures measured at 10 m depth on our six 55 m moorings, we find the OI.v2 data are warmer by 0.54 – 0.94°C , but significantly ($r > 0.95$, $p < 0.01$) cross-correlated with temperatures at 10 m.

[23] By combining the daily OISST temperatures with our in situ moored measurements, we achieve a full water column depiction of thermal stratification at the 55 m isobath moorings. Given the loss of some 10-m instruments and the problems associated with satellite detection of SSTs near the ice edge, we do not resolve the upper water column thermal stratification well in May and June, however. Stratification due to salinity is not well resolved by our mooring

measurements, but examination of our CTD casts shows that the thermocline usually coincides with the halocline except in late spring and early summer, when there is salinity stratification from ice melt.

2.6. Reanalysis Winds

[24] Winds are from the National Center for Environmental Prediction (NCEP) North American Regional Reanalysis (NARR) model hindcasts [Mesinger *et al.*, 2006]. The 1979-present NARR model output includes surface pressure, wind, temperature and ocean-atmosphere heat fluxes every three hours on a 32 km grid, and thus provides higher resolution than the 2.5° , six-hourly output of the global NCEP Reanalysis [Kalnay *et al.*, 1996] used in many studies of the Bering shelf [e.g., Ladd and Bond, 2002; Mull, 2008; Stabeno *et al.*, 2010; Danielson *et al.*, 2011]. We chose the NARR product because we are interested in resolving spatial differences in the wind field across the mooring array, and because other regional studies have found that the NARR provides good representations over the North Pacific and western Arctic [Pickart *et al.*, 2009].

2.7. Model-Generated Sea Surface Heights

[25] Since we are unable to uniformly reference the moored pressure data to a common SSH, we use a model to estimate the daily mean SSH field. That field is then in turn used to investigate the regional ocean response to variable wind-forcing. Zhang *et al.* [2010] describe the Bering Ecosystem Study ice-ocean Modeling and Assimilation System (BESTMAS) model, and we here update the integration through our mooring deployment period. The BESTMAS model was constructed to investigate the sea ice-ocean system of the Bering shelf. It is based on the coupled parallel ocean and sea ice model (POIM) of Zhang and Rothrock [2003], which consists of the Parallel Ocean Program (POP) ocean model [Smith *et al.*, 1992] and the thickness and enthalpy distribution sea ice model [Hibler, 1980; Zhang and Rothrock, 2001]. The model domain covers the northern hemisphere north of 39°N with 30 vertical levels and a horizontal grid spacing that varies from ~ 50 km in the North Atlantic to less than 4 km in the northern Bering Sea. The BESTMAS model employs the ETOPO5 bathymetric digital elevation model, and errors in ETOPO5 may contribute to errors in the calculated SSH field, since, for example, just a 5 m error represents a 20% water depth error at our shallow mooring sites.

3. Results

3.1. Shelf Conditions, July 2008 to July 2010

[26] We begin with a description of temperature, salinity, current, and wind records for the central shelf over the course of the July 2008–July 2010 mooring deployments. Examination of monthly mean conditions reveals three intervals for which seasonal averages are appropriate:

[27] a) January to March (strong winds, extensive ice cover, ice formation and brine expulsion, increasing salinity, little or no thermal stratification, and low river discharge);

[28] b) May to September (light or moderate winds, receding or absent ice cover, and increasing or strong stratification, river discharge, and shelf fresh water and heat contents); and

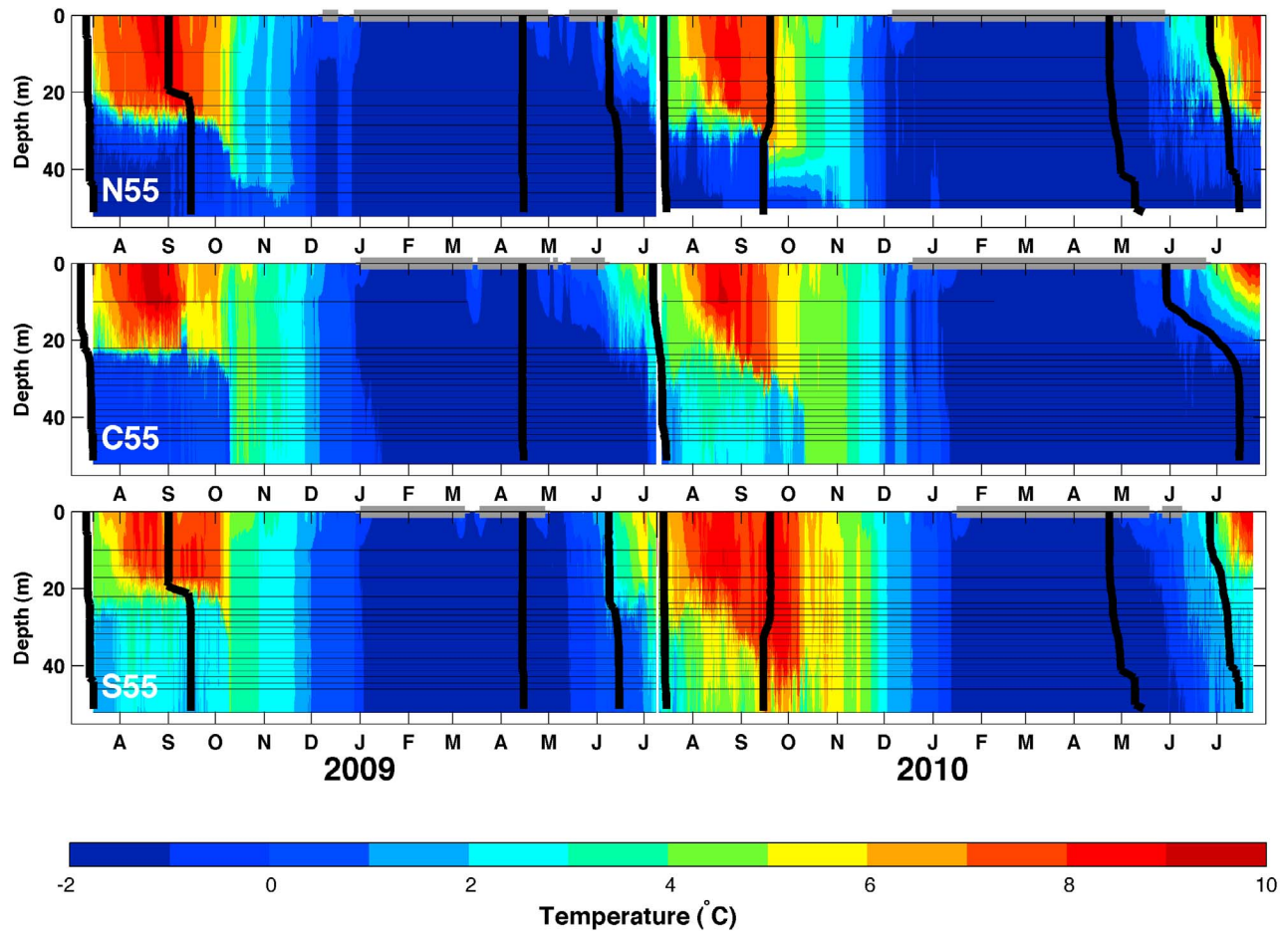


Figure 2. Contoured time series of temperature at moorings (top) N55, (middle) C55, and (bottom) S55 from July 2008 to July 2010. The contours show the annual cycle, the depth of stratification, and the timing of stratification setup and breakdown along the 55 m isobath. Thin horizontal black lines denote the depth of temperature measurements; note that the ~ 10 m depth instruments on N55 and C55 were lost partway through each deployment. Grey bars at the top denote the presence of ice with concentrations $>30\%$. Ice concentrations and surface temperatures are from the daily gridded OISST data set at the grid point closest to each mooring. Thick vertical black lines depict monthly mean observed salinity profiles taken by shipboard CTD casts within 50 km of each mooring site. The CTD salinity profiles are plotted so that their bottom-most measurement is located on the 15th day of month within which they were taken; horizontal spacing of one month is equivalent to $\Delta S = 1$.

[29] c) October to December (very strong winds and decreasing or low levels of stratification, river discharge, heat content and salinity).

3.2. Temperature and Salinity

[30] Temperatures across the array closely follow the annual solar cycle, with surface heat fluxes largely controlling the annual cycle of water temperature changes [Reed and Stabeno, 2002; Danielson et al., 2011]. Ocean temperatures are re-set each winter to the freezing point ($\sim -1.8^\circ\text{C}$) and achieve their maximum values, e.g., $\sim 10^\circ\text{C}$ near 20 m depth, in late summer or early fall. Along the 55 m isobath, late-summer water temperatures show a strongly stratified two-layer system (Figure 2), with a thermocline consistently near 20 m depth through August and September 2008, but a progressively deepening one from June into October 2009. In the fall of both 2008 and 2009, strong wind mixing and surface heat loss homogenized the water column, first at S55 and C55

(in October) and then at N55 (in November). Following fall homogenization, cooling continues, such that by the end of December (N55) and January (C55 and S55) the entire water column is at the freezing point. In half of the six observed cases, an ice cover is present before temperatures at 10 m depth attain -1.5°C , indicating that at these locations the presence of ice is often due to advection from the north [Pease, 1980]. Temperatures largely remain at the freezing point through April. In four of the six deployments along the 55 m isobath, temperatures at 20 m rose above -1°C prior to ice retreat, suggesting that ocean heat plays a role in the spring decay of the ice pack, either by advection or by absorbing solar radiation [Jackson et al., 2010].

[31] In contrast to temperature, the salinity time series depict greater spatial heterogeneity and considerable variability on weekly to monthly timescales (Figure 3). Sites N25 and C25 are closest to the coast and least saline over most of the year, with annual salinity minima occurring in fall. The

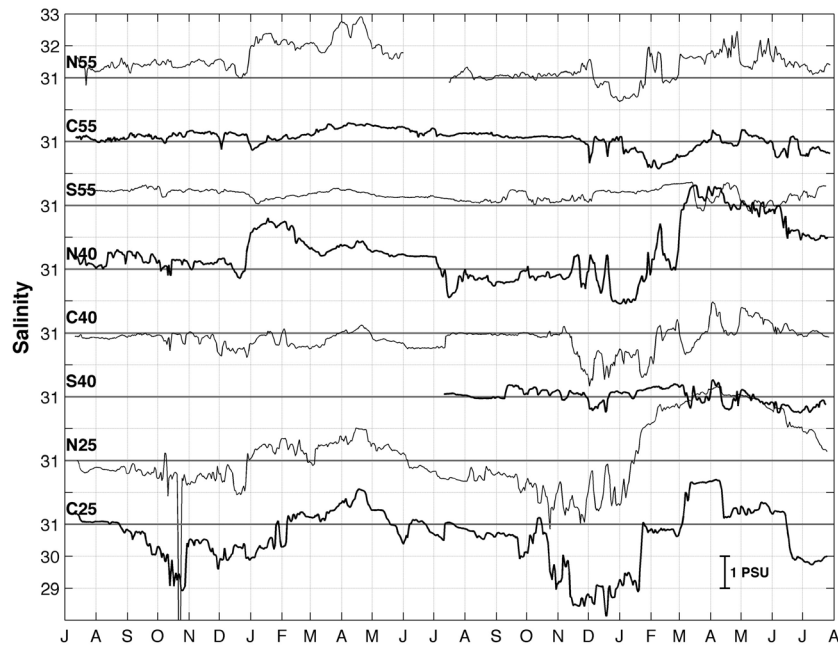


Figure 3. Daily mean salinity time series. The annual salinity minimum in fall progresses from nearshore sites (C25 and N25) to the other sites in deeper waters. All instruments were located between 17 and 25 m depth. The distance between each 31 line is $\Delta S = 2$ on the vertical axis; vertical tick marks are spaced every $\Delta S = 1$. Every other record is plotted with thick (thin) lines for clarity.

seasonal decline of salinity from late summer to a late fall/early winter annual minimum generally progresses from the shallowest (25 m) to the deepest (55 m) mooring sites. This is consistent with a westward movement of low-salinity coastal waters mixing with ambient shelf waters offshore [Danielson *et al.*, 2011]. Curiously, waters at mooring C55 remain fresher than waters at either N55 or S55 over extended intervals, e.g., July 2008–April 2009 and January 2010–April 2010, suggesting that the low-salinity signal at C55 is not due to along-isobath advection from the south or the north. Sites N40 and N55, closest to the St. Lawrence Island polynya, were the most saline ($S_{\text{MAX}} > 32.5$) during winter 2009, while in winter 2010 the most saline waters were at N40 and N25 ($S_{\text{MAX}} > 33$). For parts of each winter (but especially in 2010) the salinity decreased across the shelf from C25 to C40 and again to C55. This pattern suggests that as the fresher inshore waters were advected away from the coast, they were replaced by higher-salinity waters and/or the shallow coastal waters experienced a greater degree of salinization due to freezing, which is enhanced over shallow depths and in coastal polynyas.

[32] In both winters, higher salinities occurred at N55, N40, N25 and C25 than at C55, C40, S55 or S40. At these temperatures salinity differences control the horizontal density gradients and the salinity distribution at winter's end implies a mid-shelf salinity minimum. Such a feature would promote an anti-cyclonic geostrophic velocity field with southward flow along its eastern boundary.

3.3. Currents and Winds

[33] Figures 4 and 5 show vertically averaged, sub-tidal (35-h low-pass filtered) time series of the velocity components projected onto their major and minor principal axes of variation at each mooring site. Positive (nominally northward)

peaks in flow speeds have greater magnitude than negative (southward) excursions. Few of the time series exhibit seasonal mean velocity components that are statistically different from zero (Table 2), although all sites experience significant mean flow over averaging intervals spanning several weeks to a month or more. For example, this was seen in the mean southward flow from March to May at C40 and S40 in 2010, and the mean northward flow at all moorings in February 2009. For October–April, typical and maximum 35 h low-pass filtered half-hourly current speeds are $6\text{--}12\text{ cm s}^{-1}$ and $30\text{--}70\text{ cm s}^{-1}$ across the mooring array, respectively. Over the May–September period, these variables range from 3 to 6 cm s^{-1} and $10\text{--}30\text{ cm s}^{-1}$ (Table 2).

[34] The velocity time series show that synoptic-scale variability in the flow field is strongly seasonally modulated, with fewer peaks exceeding 25 cm s^{-1} occurring between May and September than in the rest of the year. This is also demonstrated by the fraction of the total kinetic energy accounted for by tides, viz., $61\text{--}93\%$ between October and April and $80\text{--}97\%$ between May and September (Table 2). The four dominant tidal constituents (M_2 , N_2 , K_1 , and O_1) semi-major ellipse axes amplitudes sum to $30\text{--}80\text{ cm s}^{-1}$ at 10 m depth (Table 3), greater than the filtered velocities described above.

[35] Seasonal changes in the flow field are captured by mean monthly principal axis ellipse decompositions (Figure 6). At most mooring sites, the fall, winter and early spring ellipses are larger, more elongated and more nearly parallel to the local isobaths than the ellipses of late spring through late summer. At N55, the ellipse amplitudes are less variable over the course of the year, but the ellipse orientation is more variable.

[36] Analysis of the vertical structure of the sub-tidal horizontal currents reveals that for the 55 m moorings, the mean $5\text{--}40\text{ m}$ current shear increases from 0.15 s^{-1} during May–

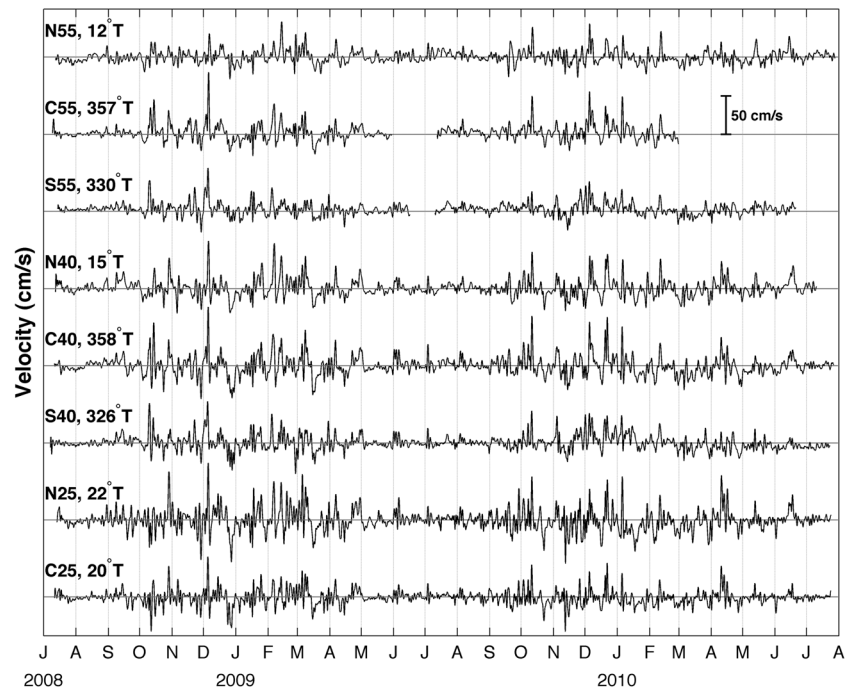


Figure 4. Time series of 35 h low-pass filtered and vertically averaged velocities along the major axis at each mooring site. Note the strongly seasonal change in variance. The axis orientation is computed from each low-pass filtered two-year time series composite and is noted next to each mooring site label. The distance between each zero line is 80 cm s^{-1} on the vertical axis.

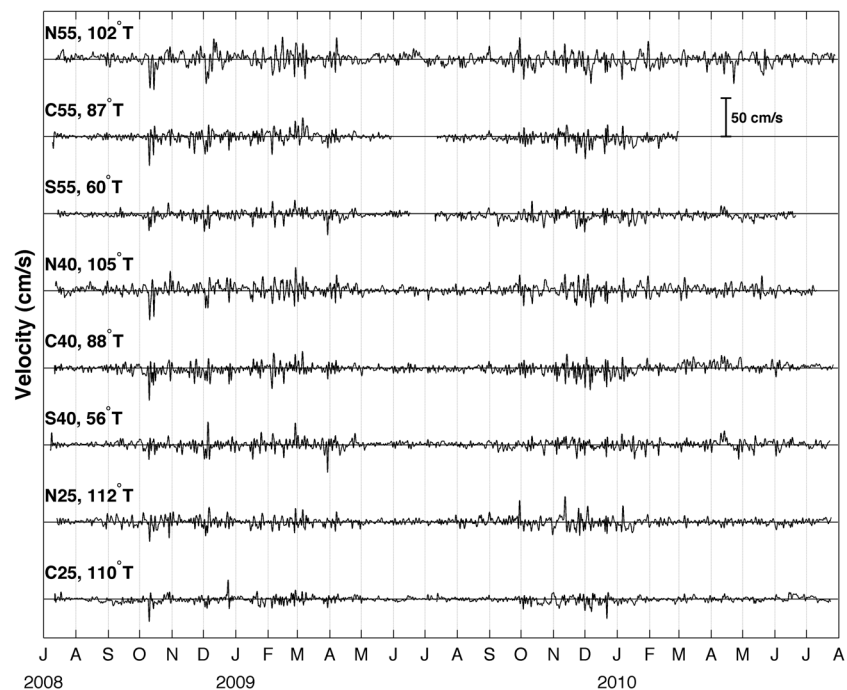


Figure 5. Time series of 35 h low-pass filtered and vertically averaged velocities along the minor axis at each mooring site. The axis orientation is computed from each low-pass filtered two-year time series composite and is noted next to each mooring site label. The distance between each zero line is equivalent to 80 cm s^{-1} on the vertical axis.

Table 2. Seasonal Current Meter Statistics at All Mooring Sites for the Water Column Vertical Average (VA) and Depths 5, 10, 20, 30 and 40 m Below the Surface^a

Mooring	Season	N	Percent of Kinetic Energy					Net Speed (cm s ⁻¹)					Net Direction (°T)					Peak Speed (cm s ⁻¹)	Mean Speed (cm s ⁻¹)	
			Tidal	VA	Inertial	VA	Mid VA	VA	Low VA	VA	5 m	10 m	20 m	30 m	40 m	VA	5 m			10 m
N55	Jan–Apr	11520	68	3	9	20	0.4	1.7	0.8	0.3	0.5	0.2	209	227	233	156	173	207	38.1	7.8
C55	Jan–Apr	8587	80	3	5	12	0.7	2.7	2.1	1.2	0.6	0.7	329	282	303	344	56	128	40.1	7.8
S55	Jan–Apr	11520	91	2	2	5	1.5	3.2	2.8	1.6	1.0	0.2	303	274	293	311	320	318	25.7	6.0
N40	Jan–Apr	11520	63	4	11	23	1.2	0.6	0.8	1.5	1.5		80	160	80	72	90	48.6	9.1	
C40	Jan–Apr	11520	80	2	5	12	1.9	2.6	2.0	1.9	1.9		169	186	174	167	166	41.5	9.8	
S40	Jan–Apr	11520	88	2	3	7	0.5	1.1	0.6	0.6	1.0		139	220	208	113	102	38.3	7.6	
N25	Jan–Apr	11520	63	3	11	22	1.4	2.3	1.4	0.9			188	198	190	167		48.6	10.6	
C25	Jan–Apr	11520	91	2	3	4	1.1	1.8	1.1	0.7			192	201	194	175		32.3	6.9	
N55	May–Sep	15459	84	2	4	10	0.5	0.9	1.1	0.8	0.5	0.5	81	70	89	79	80	302	23.7	5.5
C55	May–Sep	9332	94	3	1	3	1.4	2.1	1.7	1.7	1.2	0.4	339	313	321	349	3	308	19.5	3.4
S55	May–Sep	12467	95	2	1	3	3.0	4.0	3.8	2.9	2.8	1.4	328	306	318	327	337	325	13.0	4.2
N40	May–Sep	14582	84	5	3	8	0.9	0.6	0.6	1.1	1.0		29	345	26	35	39	23.9	5.0	
C40	May–Sep	15426	94	2	1	3	0.4	0.9	0.7	0.4	0.5		308	275	305	316	182	22.8	4.7	
S40	May–Sep	15483	95	2	1	2	0.8	1.0	0.8	0.8	0.7		140	165	152	137	139	17.3	3.9	
N25	May–Sep	19000	88	3	4	5	0.7	0.2	0.6	0.8			104	159	91	97		33.4	5.2	
C25	May–Sep	15329	97	1	1	1	0.3	0.9	0.4	0.2			220	214	235	289		17.4	3.5	
N55	Oct–Dec	8832	66	4	9	21	1.5	2.2	2.1	1.7	1.0	1.1	307	294	302	312	318	296	36.5	8.8
C55	Oct–Dec	8832	73	2	8	17	3.5	4.6	4.5	4.0	2.9	2.3	336	322	325	336	348	346	65.3	9.4
S55	Oct–Dec	8832	84	2	4	11	4.1	4.7	4.9	4.4	3.8	3.0	327	310	318	328	334	336	45.8	8.2
N40	Oct–Dec	8832	61	5	11	24	0.8	0.5	0.3	1.0	1.4		108	215	113	94	111	50.4	10.0	
C40	Oct–Dec	8832	73	3	8	16	3.0	4.4	3.9	2.8	1.7		273	269	272	278	269	61.5	11.8	
S40	Oct–Dec	8832	84	2	5	9	1.9	1.9	2.2	2.1	1.7		347	315	329	352	11	46.3	8.8	
N25	Oct–Dec	8832	63	4	14	20	1.1	1.5	0.9	1.7			183	235	191	152		59.1	11.6	
C25	Oct–Dec	8832	88	2	4	5	2.1	3.8	2.4	0.3			218	219	221	209		41.9	8.3	

^aN is the number of half-hour samples obtained over the course of the deployments. Net speed and direction computed for 35-h LPF data. Percent tidal kinetic energy is determined from yearly harmonic tidal analyses at frequencies resolved with signal-to-noise greater than or equal to 10. The high-frequency band contains frequencies remaining after passing through a 35-h high-pass filter, less the resolved harmonic analysis tidal portion. Mid-frequencies are band-pass filtered over the 35–100 h range; low frequencies are low-pass filtered at 100 h. Net speeds greater than zero at the 95% confidence level are given in bold type, based on a decorrelation time scale of 48 h.

December to 0.21 s⁻¹ during January–April, with these means significantly different at the 95% confidence level. In contrast, at the 25 m moorings the 5–20 m shear was largest in fall (0.44 s⁻¹), smallest from May–September (0.29 s⁻¹) and intermediate in January–April (0.37 s⁻¹), with these means significantly different from one another.

[37] Winds, strongest in fall months (Figure 7), reflect the evolution, location and strength of storms associated with the Aleutian Low [Wilson and Overland, 1986; Pickart et al., 2009]. The 3-hourly wind record from the NARR grid point closest to site C55 contains 20 wind speed peaks with magnitude ≥ 15 m s⁻¹. Of these, 17 occurred in October, November or December 2008 and 2009; the remaining three were in July and August 2009. Winds do not strongly favor one orientation: only 57% of the variance is directed along the principal axis. Rotary coherence calculations at all grid points across the shelf with respect to the grid point closest to 60°N, 170°W reveals that coherence-squared values of 0.8 occur within a radius of ~ 200 km for long (≥ 32 h) periods, but only within ~ 100 km for shorter periods (Figure 8). Thus, over short time scales the wind field is not uniform across the mooring array, which spans 3 degrees of latitude and 4 degrees of longitude.

[38] Figure 9 summarizes averages of the current meter and wind records for the periods January–April, May–September and October–December. On average, winds are northerly during each period, and strongest in fall and weakest in summer. Vertically averaged currents are generally northward along the 55 m isobath. In contrast, the flow along the 25 m isobaths is southward. Here the mean vectors, along with

those at N40 and C40 suggest a clockwise circulation over the inner half of the central shelf. The currents at S40 are weakly southeastward in winter and summer, but become northwestward and strengthen in fall. Mooring C40 vectors are remarkably different from those at the 55 m moorings, but are consistent with the flow field depicted by the N40, N25 and C25 moorings.

[39] In summary, weekly and shorter variations in the flow field are large with respect to seasonal and annual means, but temperature and salinity fields are dominated by variability on monthly to annual time scales. Seasonal averages of the wind and current fields show that near-surface (<10 m) waters flow predominantly westward. Vertically averaged inner shelf currents are southward or westward during the fall, winter and early spring. Consistent with this flow, low salinities are first observed at the nearshore (shallow) sites in the fall and early winter, and only later in winter at the offshore moorings. However, in winter the moorings nearest to St. Lawrence Island and the Alaskan coast are more saline than at the other moorings.

[40] The flow field is not horizontally uniform and the measurements do not suggest that the surface Ekman drift is locally compensated by a subsurface flow. Consideration both of along-shelf variations in the flow field and of the dynamics of surface and bottom boundary layers are therefore necessary to construct an adequate picture of the circulation field.

3.4. The Momentum Balance

[41] We next examine the vertically integrated equations of motion in order to identify the relative importance of the

Table 3. Tidal Ellipse Harmonic Parameters for the M₂, N₂, K₁ and O₁ Constituents Based on Non-overlapping 29-day Analyses of the Current Data at 10 m Depth^a

Constituent	Mooring Name	N	MAJ (cm s ⁻¹)	σ_{MAJ} (cm s ⁻¹)	Min (cm s ⁻¹)	σ_{min} (cm s ⁻¹)	I (deg)	σ_I (deg)	G (deg)	σ_G (deg)
M2	N55	25	15.9	1.0	-12.4	0.8	168	4	24	7
	C55	18	23.3	0.6	-15.0	0.7	30	3	144	4
	S55	22	25.9	1.2	-20.9	1.2	42	3	114	6
	N40	24	21.0	1.4	-7.7	1.1	172	6	29	14
	C40	25	30.9	2.1	-17.3	1.9	28	5	148	4
	S40	25	28.2	1.8	-22.9	1.6	40	4	118	5
	N25	27	22.3	1.8	2.5	1.6	159	3	12	4
	C25	25	42.8	1.6	-7.7	1.3	11	3	161	2
N2	N55	25	4.3	0.7	-3.2	0.6	171	8	258	144
	C55	18	6.3	1.1	-3.8	0.8	31	7	91	11
	S55	22	6.8	1.0	-5.1	0.9	41	7	61	15
	N40	24	5.5	1.0	-1.8	0.8	172	9	260	142
	C40	25	8.1	1.3	-4.2	1.1	27	8	97	12
	S40	25	7.2	0.9	-5.4	0.9	43	8	60	11
	N25	27	5.9	0.8	1.1	0.6	159	7	319	11
	C25	25	10.9	1.6	-1.5	0.5	13	4	109	10
K1	N55	25	5.9	1.2	-4.8	0.9	136	29	174	33
	C55	18	9.2	1.8	-5.3	1.2	90	5	209	16
	S55	22	12.1	2.4	-5.1	1.0	128	2	174	14
	N40	24	7.2	1.3	-4.0	0.8	47	7	275	15
	C40	25	13.6	2.6	-5.9	1.2	83	5	215	15
	S40	25	16.2	3.1	-5.1	1.1	124	2	177	13
	N25	27	14.6	2.7	-3.1	0.6	62	2	259	13
	C25	25	15.0	2.8	-2.7	0.7	67	4	215	13
O1	N55	25	3.9	0.4	-2.8	0.4	134	15	157	14
	C55	18	5.9	0.4	-3.0	0.4	99	4	179	5
	S55	22	8.1	0.5	-3.0	0.3	130	3	149	4
	N40	24	4.3	0.4	-2.5	0.2	65	10	229	11
	C40	25	8.5	0.5	-3.3	0.5	88	5	184	4
	S40	25	10.6	0.7	-3.1	0.6	126	3	148	3
	N25	27	8.9	0.8	-2.2	0.4	68	3	216	5
	C25	25	8.8	0.6	-1.5	0.4	74	5	177	5

^aThe first three columns list the tidal constituent name, the mooring name, and the number (N) of 29-day segments that comprise each summary statistic. The last eight columns contain the mean and standard deviations (σ) of the semi-major axis (MAJ), the semi-minor axis (min), the inclination (I) and the Greenwich phase (G). Negative values of the semi-minor axis denote clockwise rotation; positive values denote counter-clockwise rotation.

various sources and sinks of momentum. Following *Brink* [1998], we vertically integrate the linearized horizontal momentum balance (1), prescribing the along-shelf direction with (y , V), positive along the northward-directed principal axis of variation (Figure 4), and the cross-shelf direction oriented 90° to the right with (x , U).

$$\begin{aligned} U_t - fV &= -\frac{P_x}{\rho_w} + \frac{1}{\rho_w} (\tau_0^x - \tau_B^x) \\ V_t + fU &= -\frac{P_y}{\rho_w} + \frac{1}{\rho_w} (\tau_0^y - \tau_B^y) \end{aligned} \quad (1)$$

[42] The upper line of (1) is the cross-shelf momentum balance; the lower line is the along-shelf momentum balance. From left to right in (1), the five terms represent local and Coriolis accelerations, horizontal pressure gradients, and surface and bottom stresses. The parameters include the Coriolis frequency (f) and water depth (h) appropriate for each site and the water density ($\rho_w = 1025.3 \text{ kg m}^{-3}$). The surface and bottom stress terms are

$$\begin{aligned} \tau_0^x &= \frac{C_d \rho_a}{h} W_u |W|, & \tau_0^y &= \frac{C_d \rho_a}{h} W_v |W| \\ \tau_B^x &= \frac{\rho_w r}{h} U, & \tau_B^y &= \frac{\rho_w r}{h} V \end{aligned} \quad (2)$$

where the neutral drag coefficient C_d is computed following *Large and Pond* [1981] and is doubled [*McPhee*, 1980] for intervals when the mooring site is covered with ice (concentration $\geq 30\%$). The linear bottom friction coefficient r is set to $5 \times 10^{-4} \text{ m s}^{-1}$ after *Lentz and Winant* [1986]; air density (ρ_a) is 1.22 kg m^{-3} ; and the wind velocity vector $W = W_u + iW_v$ uses 3-hourly NARR wind velocities from the grid cell closest to each mooring site. The momentum balance is computed with the raw (unfiltered) time series of velocity and wind speeds. Each term is subsequently low-pass filtered (35 h cutoff) in order to focus only on the coherent portion of the flow field (as justified below in section 3.5). Nonlinear advective terms are neglected, because the Rossby number $R_o = U/fL \ll 1$ for characteristic subtidal speed and length scales of 10 cm s^{-1} and 100 km , respectively. The horizontal pressure gradient cannot be estimated directly from our data and is therefore determined as the residual in the momentum balance. The approach used here depends on the surface and bottom drag coefficients. Sensitivity analyses show that a factor of two change in the surface and/or bottom stress drag coefficients alters the magnitude of any seasonal mean pressure gradients by $\sim 5\text{--}10\%$ over the 40 m and 55 m isobaths and by $\sim 10\text{--}30\%$ for sites along the 25 m isobath. Maximum changes for these two depth groupings are 20% and 40% , respectively. The largest changes are associated with the along-shelf momentum balances.

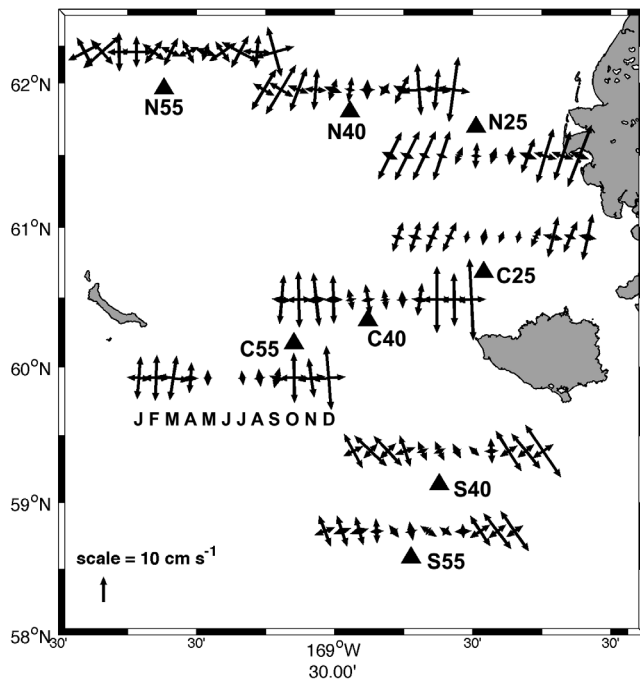


Figure 6. Mean monthly decomposition of the flow field into ellipses denoting the along- and cross-principal axis of variation for currents at 20 m depth. Each set of axes begins with January on the left and ends with December on the right as labeled for C55. Most sites exhibit an annual modulation in magnitude and show relatively little variation of direction among months; N55 is a notable exception. Due to battery failures both years at C55, axes are missing in June for this mooring. Triangles denote the associated mooring location for each set of axes.

[43] An example of all terms in (1) evaluated at one site (C25), which is representative of the other sites, is shown in Figure 10. The balance is primarily geostrophic in both the along-shelf and cross-shelf directions, because only the pressure gradient residual is large enough to balance the Coriolis term. Short intervals during which the other terms are important, or even dominant, include energetic wind events and transitions between positive and negative along-shelf flow, when our assumption of linearity is unlikely to hold. To quantify the relative importance of the terms in (1), we

compute the seasonal mean root-mean square (RMS) magnitude of each term and scale these as a fraction of the combined total at each site (Figure 11). For along-shelf currents, the Coriolis term is nearly balanced by the cross-shelf pressure gradient during all seasons, although surface stress can account for up to 20% of the balance. Stronger winds in fall generate surface stresses slightly larger than those of winter, despite enhanced frictional coupling by winter ice. Bottom stress and local accelerations together represent <10% of the cross-shelf momentum budget. The contribution from bottom stress terms is proportionally larger (as expected) at the shallow sites, due to h in the denominator of (2). The pressure gradient and Coriolis terms also dominate the along-shelf momentum balance, however the local acceleration, wind stress and bottom friction terms can account for 15–40%, depending on location and season. The momentum balance averaged across all mooring sites varies little among seasons despite seasonal changes in the RMS value of the individual terms (Table 4). This suggests the importance of the wind in setting up the SSH gradients, regardless of season.

[44] In addition to the barotropic response of the shelf to SSH gradients, horizontal variations in the thermohaline fields may play a role in forcing the circulation field. We use late winter/spring and late summer/early fall CTD survey data collected between 2006 and 2010 to examine the mean seasonal changes of the dynamic topography, noting that the shallow water depths preclude referencing the computations to a realistic level of no motion. We measure in situ shear with the current meters, but direct comparison to the baroclinic shear is difficult due to overlap between the surface Ekman layer, the bottom Ekman layer and the geostrophic shear.

[45] Between spring and the end of summer, nearshore (shallow) waters warm and freshen proportionally more than mid-shelf waters. In addition, the cold, saline sub-pycnocline waters on the middle shelf (including the cold pool) are dense and will therefore tend to stagnate on weakly sloping continental shelves [Hill, 1996]. By late summer, the juxtaposition of low-density nearshore waters and the denser cold-pool waters over the mid-shelf promotes a northward baroclinic flow along the eastern side of the cold pool. This hydrographic structure is evident in previous cross-shelf transects as well [Coachman, 1986; Kachel et al., 2002; Danielson et al., 2011]. We therefore average the late summer-early fall BASIS hydrography from 2006 to 2009 to generate the 0–30 db dynamic topography and associated geostrophic

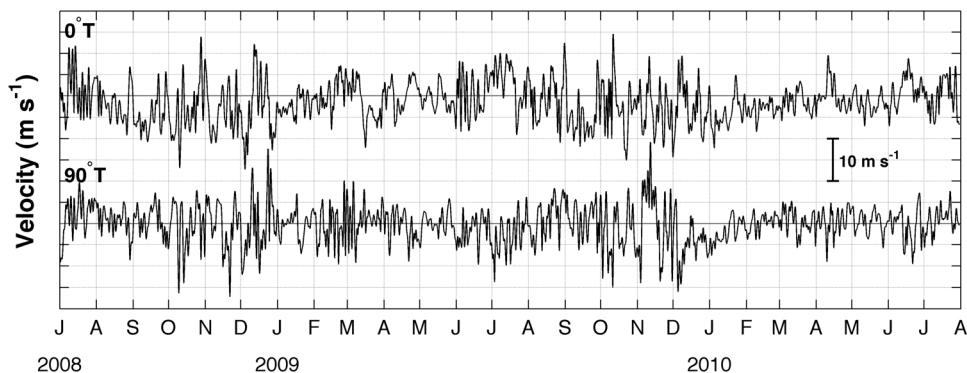


Figure 7. North-south (0°T) and east-west (90°T) wind components at the NARR grid point closest to mooring C55. For consistency with Figures 4 and 5, the time series shown here are 35 h low-pass filtered.

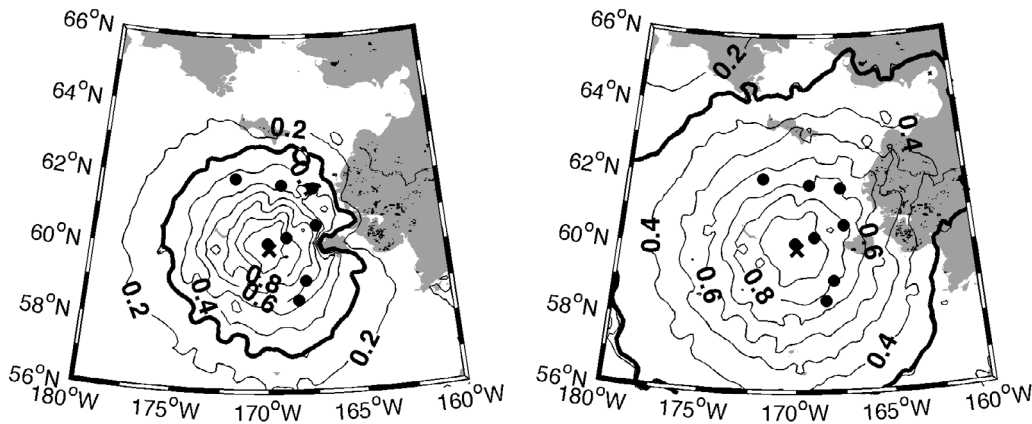


Figure 8. Coherence-squared of the (unfiltered) NARR wind field with respect to NARR winds at a reference site located at 60°N, 170°W for (left) short (<32 h) and (right) long (>32 h) periods from July 2008 to July 2010. Short period fluctuations have much smaller decorrelation length scales than those of longer period. The reference site is marked by x and the mooring sites by dots. The contours are plotted at intervals of 0.1, beginning with $\gamma^2 = 0.9$ for the innermost closed contour around the reference point. The thick black contour denotes $\gamma^2 = 0.31$, the level of statistically significant coherence at the 95% confidence level.

vectors shown in Figure 12 (right). South of, but near, St. Lawrence Island, the relatively salty and cold waters advected eastward from the Gulf of Anadyr are denser than waters farther south. The resulting pressure gradient corresponds to a geostrophic eastward flow toward Shpanberg

Strait, where the current veers northward upon encountering the fresher and warmer waters near the Alaska coast.

[46] In March, April and May, mid- and inner shelf waters are nearly isothermal so that the late winter dynamic topography is determined primarily by salinity. Upon combining

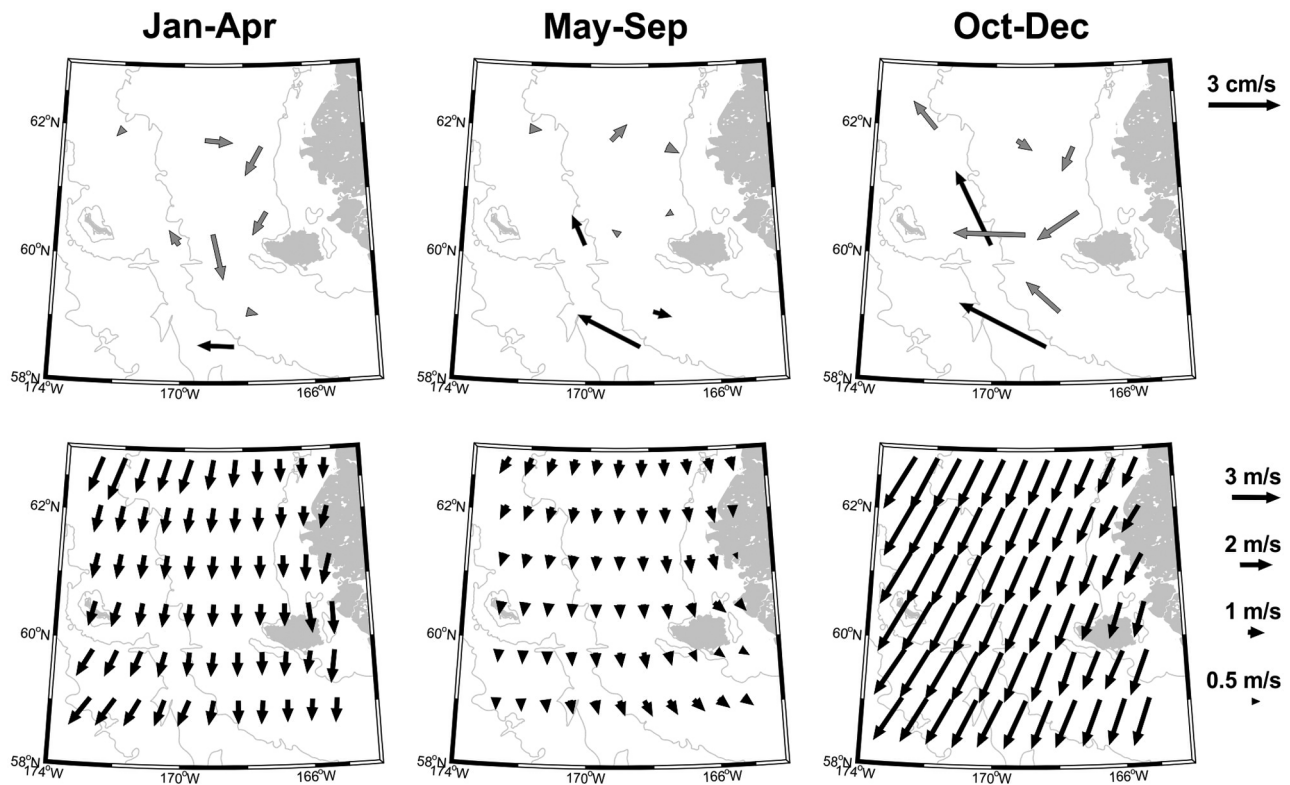


Figure 9. Seasonal averages of (top) vertically averaged currents and (bottom) winds in the study region. Black current vectors are significantly different from zero. The ice-covered January to April period is on the left, the stratified May to September period in the middle, and the strong mean wind October to December period is on the right. Wind vectors from every 4th NARR grid cell are displayed. Scale vectors for each set of panels are shown on the right-hand side.

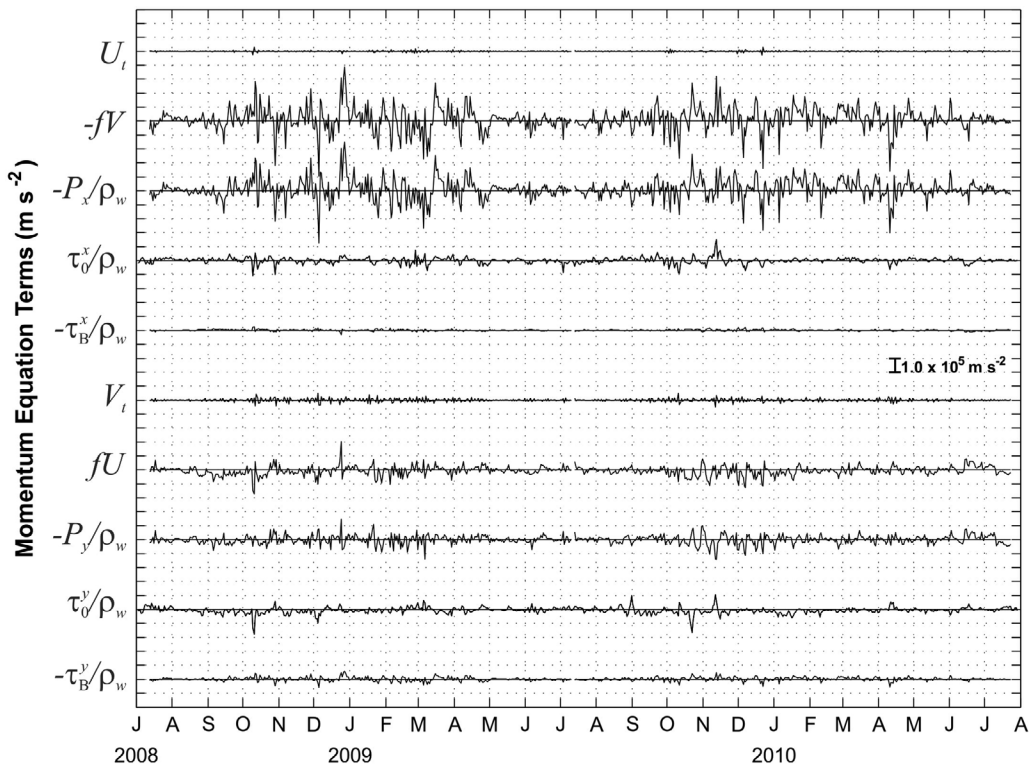


Figure 10. Time series of each term of the 35-h low-pass filtered, vertically integrated equations of motion (equation (1)) at site C25. Zero lines are spaced every $5 \times 10^5 \text{ m s}^{-2}$ along the vertical axis and tick marks are every $1.0 \times 10^5 \text{ m s}^{-2}$.

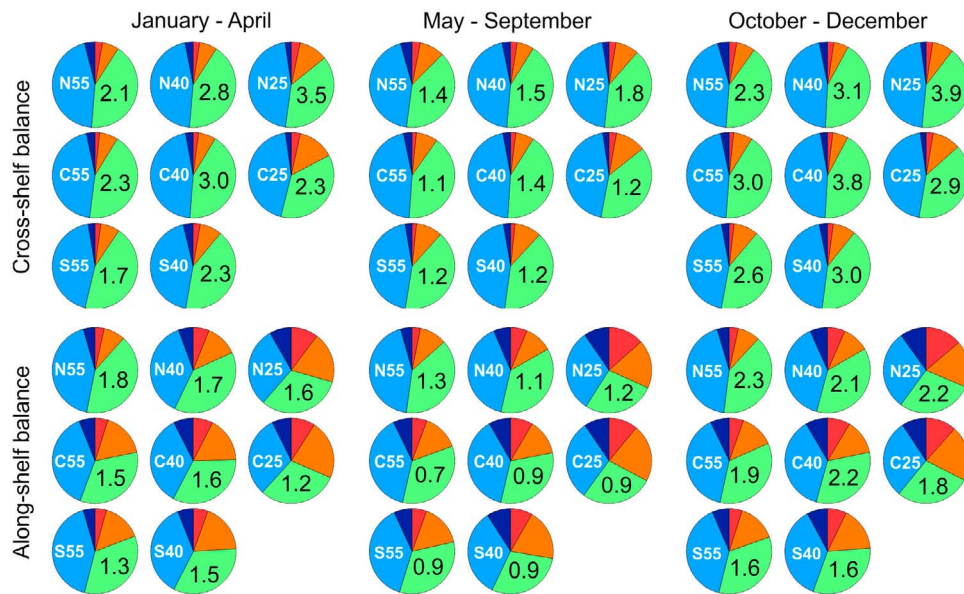


Figure 11. Pie charts depicting the relative contribution of the momentum balance terms to each site’s total based on 35-h low-pass filtered RMS magnitudes. The top three rows depict the cross-shelf momentum balance and the lower three rows the along-shelf momentum balance (equation (1)). The left three columns show January–April, the middle May–September, and the right October–December. Colors represent the Coriolis (light blue), local acceleration (dark blue), bottom stress (red), surface stress (orange) and horizontal pressure gradient (green) terms, respectively. Numbers denote the magnitude of the horizontal pressure gradient term multiplied by $10^5 \text{ m}^2 \text{ s}^{-2}$. Reduced magnitudes at all sites are evident in May–September but the relative importance of each term changes only slightly. The cross-shelf momentum balance shows little dependence on bottom friction or local accelerations.

Table 4. Relative Contribution of Individual Momentum Balance Terms to the 35-h Filtered Vertically Integrated Equations of Motion, Averaged Across All Mooring Sites and Separated by Season^a

	Averaging Interval	RMS Total ($\times 10^5 \text{ m}^2 \text{ s}^{-2}$)	Local Acceleration	Coriolis	Horizontal Pressure Gradient	Surface Stress	Bottom Stress
Cross-shelf Balance	Jan–Apr	2.5	4%	46%	43%	6%	2%
	May–Sep	1.3	4%	44%	41%	8%	3%
	Oct–Dec	3.1	4%	45%	40%	9%	2%
Along-shelf Balance	Jan–Apr	1.5	9%	37%	35%	11%	8%
	May–Sep	1.0	8%	36%	34%	15%	6%
	Oct–Dec	2.0	9%	37%	32%	15%	7%

^aThe column labeled RMS total depicts the sum of all five terms in the momentum balance multiplied by 10^5 ; the other columns show the fraction of the RMS explained by each of the five components of equation (1). Despite large seasonal changes in the total kinetic energy, the relative contributions of the individual terms remain approximately the same.

CTD profiles from the March to mid-June cruises of 2006–2010, we find a geopotential height minimum south of St. Lawrence Island and along the Alaskan mainland coast and a maximum farther offshore (Figure 12, left). This reverses the late summer cross-shelf baroclinic pressure gradient so that by the end of winter inner and mid-shelf waters have a southward geostrophic tendency. Similar plots from individual year CTD data are generally consistent with this 5-year climatology. We note that a late winter salinity minimum over the middle southeastern shelf was also observed in an April 1979 cross-isobath transect [Coachman, 1986].

[47] The baroclinic currents computed from these five years of shipboard data indicate that the surface (relative to 30 db) geostrophic vectors are of the same magnitude as the observed vertically averaged seasonal mean flow (Figure 9), so that the baroclinic field appears dynamically important. Whereas

the northward baroclinic velocity vectors in summer oppose the mean southward (but weak) winds, the southward baroclinic vectors in winter are aligned with the prevailing winds. The late winter-spring and late summer-fall means in Figure 12 probably represent the strongest baroclinic pressure gradients, because they include the cumulative effects of cooling and salinization through winter and warming and freshening through summer. Very likely the baroclinic velocity field is therefore smaller in mid-winter and mid-summer.

[48] The total pressure gradient is the sum of the barotropic pressure gradient ($\nabla P_{\text{barotropic}}$) due to wind-forced convergences and divergences and the baroclinic pressure gradient ($\nabla P_{\text{baroclinic}}$). We earlier computed $\nabla P = P_x + iP_y$ as the momentum balance residual. Here, we scale the baroclinic contribution against the other terms in equation (1). From Figure 12 and from inspection of the gridded velocity field

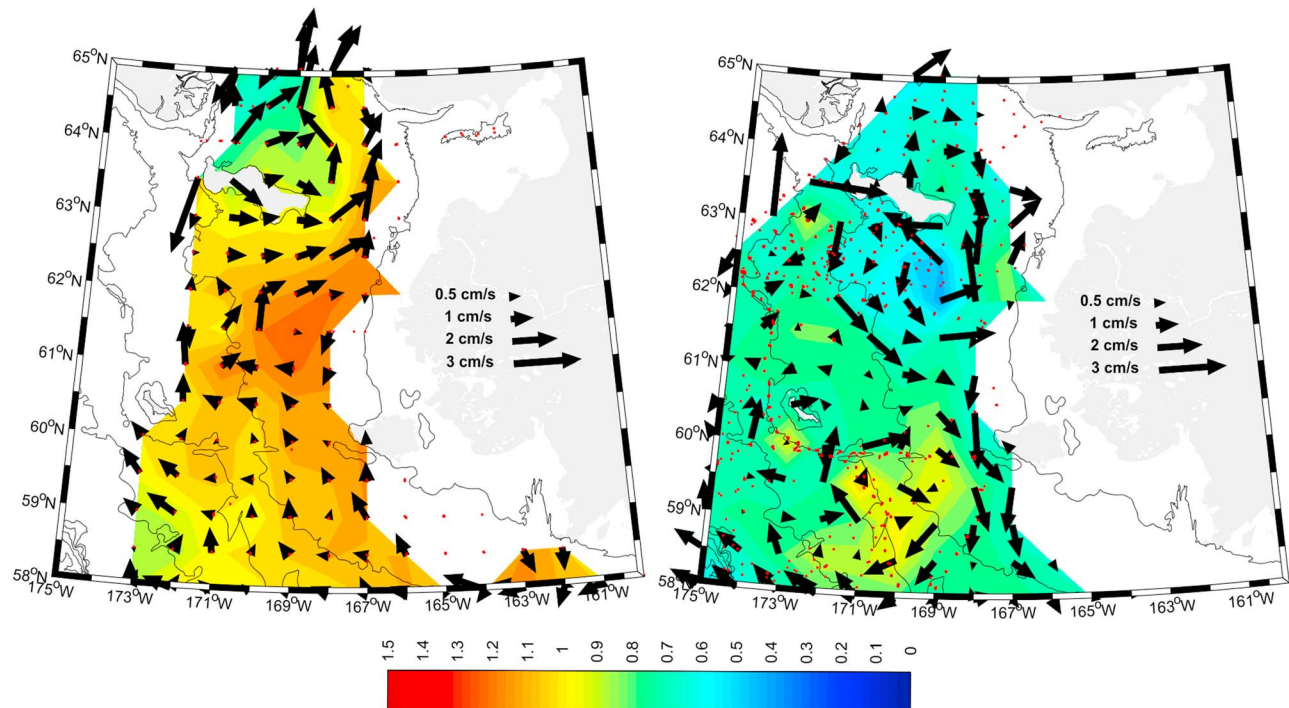


Figure 12. Geopotential height anomaly (color shading) and geostrophic current vectors computed over 0–30 db for 2006–2010 (left) late winter and early spring and (right) late summer and early fall. Over much of the central shelf, the vectors depict a northward velocity tendency at the end of summer and a southward tendency at the end of winter: the cross-shelf baroclinic pressure gradient reverses sign between these periods. Small red dots depict the location of CTD casts.

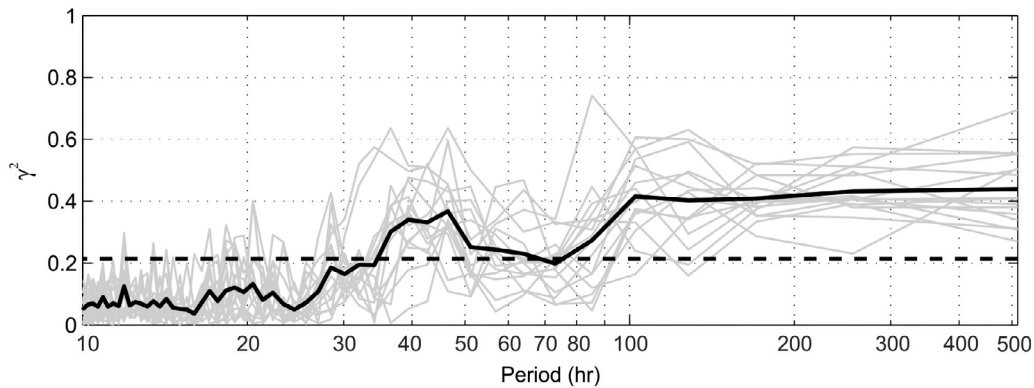


Figure 13. Coherence-squared (γ^2) between NARR winds at each mooring site with currents measured at 5 m depth. Sixteen comparisons (thin light traces) are shown, one for each yearlong deployment at each of the eight mooring sites. The thick dark line is the average of all sixteen. The dashed line shows the average significance level.

for each individual cruise, we find that the typical (maximum) 0–30 db geostrophic velocity is about 1 (3) cm s^{-1} and $\nabla \mathbf{P}_{\text{baroclinic}}$ is about 1 (3) $\times 10^{-6} \text{ m s}^{-2}$. In late winter and late summer, $\nabla \mathbf{P}_{\text{baroclinic}}$ is therefore generally larger than the local accelerations, wind stress, and bottom friction, but 60–90% smaller than the Coriolis term. Comparing these results with the pressure gradient residual in equation (1) implies that $\nabla \mathbf{P}_{\text{barotropic}}$ is 2–8 times greater than $\nabla \mathbf{P}_{\text{baroclinic}}$. We note also that the SSH field changes rapidly in response to synoptic winds, while the temperature and salinity fields evolve more slowly. Hence, the cross-shelf baroclinic pressure gradient can alternately oppose and reinforce the changing barotropic pressure gradient.

[49] In summary, the along- and cross-shelf momentum balances at all sites are predominantly geostrophic in response to sea surface height gradients. However, changes in the cross-shelf thermohaline structure, current and wind velocities, and sea ice seasonally modify the cross-shelf momentum balance. In the next section, we examine the vertical and horizontal structure of the current field and its relation to the wind field, and we show that Ekman dynamics lead to a flow field that is highly sensitive to the wind direction and the resultant sea surface topography.

3.5. Co-variability of the Current, Wind and SSH Fields

[50] We next examine the temporal and spatial structure of the flow field and their relation to winds. Following this, we use the BESTMAS model to relate wind and current variations to the structure of the SSH field.

[51] Prior evaluations of the wind-current relationship found weak to moderate correlations [Schumacher *et al.*, 1982; Muench *et al.*, 1988; Danielson *et al.*, 2006] over the central shelf, although these estimates were primarily based on time domain correlations. Here we first examine the rotary coherence structure (frequency domain relations) between near-surface currents and winds across specific portions of the frequency spectrum. All coherence computations are based on non-overlapped windows truncated with a Hanning tapering function. The velocity records used for the coherence computations were de-tided using harmonic analysis applied to monthlong segments.

[52] While energetic flows are roughly coincident across the array (Figures 4 and 5), close examination of differences in the phasing and magnitude of currents suggest a flow field that evolves with considerable spatial structure over short time scales and whose relative magnitude and phasing vary among the various energetic flow events. Figure 13 shows that at high frequencies (periods < 35 h), winds and currents at 5 m depth are incoherent across the array. At low frequencies (periods > 100 h) winds and currents are significantly coherent on average, but with the coherence-squared (γ^2) ~ 0.4 . Inspection of the phase shows that the wind leads the 5 m current by 45–90° for all periods greater than ~ 30 h. The wind-current coherence peak in Figure 13 at ~ 40 h corresponds to a corresponding maximum in wind energy. Analysis of vertically averaged currents and the wind shows the same frequency dependence as for the 5 m currents, although γ^2 in the low-frequency band is smaller (~ 0.3).

[53] Based on Figure 13, we divide the velocity time series into three frequency bands and use vertically averaged currents to compute γ^2 between each mooring pair, shown in Figure 14 as a function of separation distance. The high frequency band (13–22 h) was formed by band-pass filtering the velocity records after subjecting them to harmonic de-tiding of monthlong segments. This band contains the inertial (13.8 h at 60°N) and near-inertial periods. The mid-frequency band spans periods of 32–102 h and the low-frequency band 128–512 h.

[54] The high-frequency portion of the spectrum has low coherence ($\gamma^2 < 0.4$) (with a slight linear dependency on separation), and most correlations are not significant at the 95% level. The mid-frequency band shows that $0.4 < \gamma^2 < 0.65$ at sites within 100 km of each other and these are all significant. Moreover, most sites within 200 km of each other are also coherent, but only weakly so. The low frequency band is coherent for nearly all mooring combinations; values range from $0.6 < \gamma^2 < 0.8$ at 50–100 km separation to $\gamma^2 < 0.5$ at separations > 250 km. With an average separation distance of ~ 85 km between adjacent moorings, the mooring array therefore resolves a large portion of the flow field at synoptic to fortnightly time periods.

[55] We next examine the vertical structure of current co-variability in the mid-frequency portion of the spectrum.

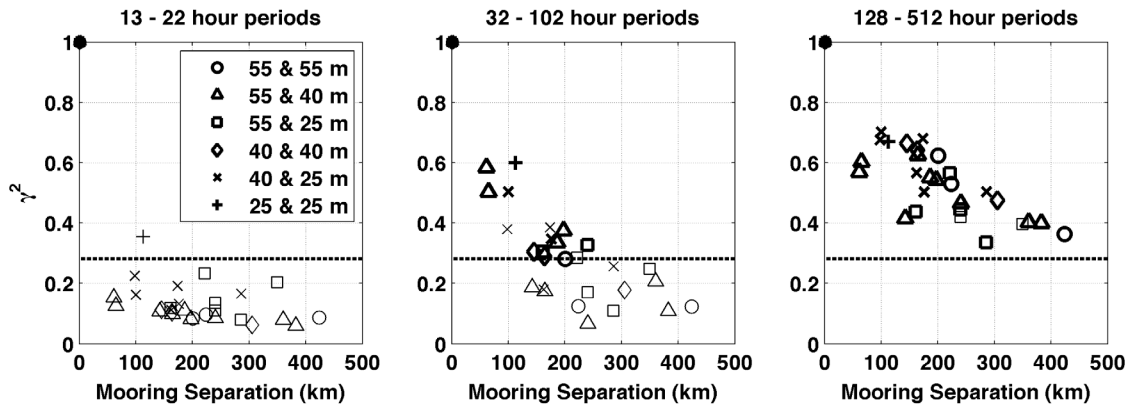


Figure 14. Rotary coherence-squared (γ^2) of vertically averaged currents from all mooring pair combinations. Symbols denote the depth combination for each comparison (see legend). Symbols plotted with thick lines are significantly coherent at the 95% confidence level and the mean level of significance for all combinations is plotted with a dotted line.

At the shallow (25 m) sites the currents are coherent over the entire water column, although there is some seasonal variation (Figure 15). Over the 40 and 55 m isobaths, the currents are vertically coherent between 5 m and 30 m depth ($\gamma^2 > 0.6$) during fall, winter and early spring, coincident with weak stratification and strong winds (see Figures 2 and 9). Coherence decreases ($\gamma^2 < 0.6$) between mid- spring and late summer below 20 m depth, consistent with Figure 2 and other observations that find the upper mixed layer is typically between 15 and 30 m depth [e.g., *Ladd and Stabeno, 2012*]. Slight differences in coherence between the fall and winter are statistically insignificant, but suggestive of the influence of ice cover.

[56] We now turn to the SSH field. Pressure measurements made at seven of the eight mooring sites were de-tided with a 35-h low-pass filter and converted to equivalent SSH fluctuations (Figure 16). Variations from the record-length means greater than 0.5 m occur most often in fall, winter, and spring. The largest SSH excursions are at the 25 m sites, where storm surges of ~ 1 m are seen in December 2009. Record-length cross-correlations between the BESTMAS

model and observed SSH fields show that the model captures from 31% (at N55) to 61% (at N40) of the observed variability (Figure 16). With the exception of site N40, correlations between the observed and modeled SSH fields are stronger between October and May than during June–September (Table 5). The barotropic Rossby deformation radius $R_{bt} = (gH)^{1/2} f^{-1}$ varies from 120 km for water 25 m deep to 160 km for 40 m depths and 180 km for 55 m. For comparison, N25 (N40, N55) is ~ 70 km (170 km, 300 km) due west of the Alaskan mainland. The BESTMAS model and the above scaling indicates that mooring N55 was in a region with relatively small horizontal SSH gradients, so the lower levels of correlation here are not surprising.

[57] The time of maximum correlation (τ) between the wind and observed pressure fluctuations varies slightly with water depth (not shown), so that at the 25 m and 40 m sites the SSH tends to lag the winds by 0–8 h, with $0.2 < r^2 < 0.5$, while at the deeper sites $r^2 < 0.3$ and the maximum correlation occurs with a lag of up to 20 h.

[58] Table 4 and Figure 11 show that the momentum balance is not strongly seasonally variable. Therefore, based on the

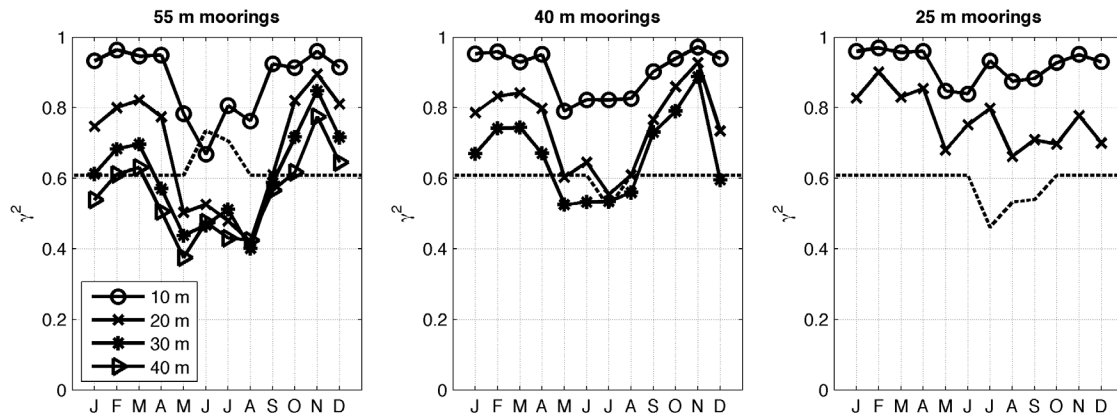


Figure 15. Rotary coherence-squared (γ^2) between currents at 5 m and those at 10 m, 20 m, 30 m and 40 m depths for the (left) 55 m, (middle) 40 m and (right) 25 m moorings for the mid-frequency band (32–102 h) as a function of calendar month. The 95% significance level for coherence is shown by the dotted line.

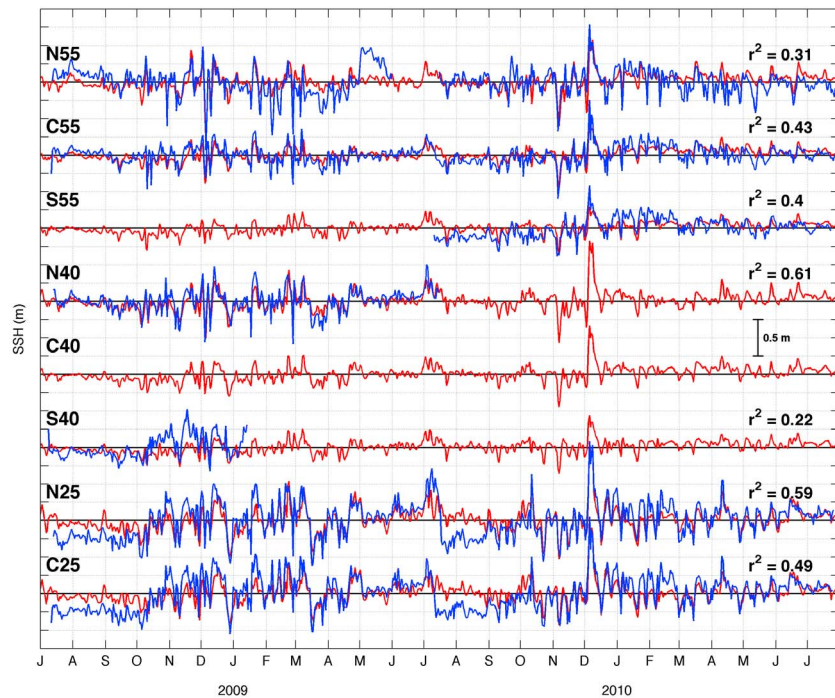


Figure 16. SSH time series. Moored pressure records are 35-h low-pass filtered, demeaned, and converted to equivalent elevation changes (blue lines); BESTMAS modeled SSH (red lines) are daily values at each mooring site. The record-length cross-correlations squared are denoted along with each time series. All correlations are statistically significant at the 95% level except for the short record at mooring S40. On the vertical axis, the distance between the zero line for each time series is equivalent to 1 m SSH change, with tick marks every 0.25 m.

direction of the mean regional wind vector (formed by equally weighting the NARR wind time series from all eight mooring sites), we made record-length averages of the mean wind vector, the BESTMAS SSH field, and the moored current measurements (Figure 17). Because the model output is daily, and because of the lagged wind-SSH relation, we made 24-h averages of the wind vector preceding each current measurement to determine the wind direction bins used in assembling the panels of Figure 17.

[59] Changes in wind velocity impact currents through SSH gradients (Figure 17). The near-surface (5 m and 10 m depths, red and yellow vectors) flow field is typically aligned to the right of the wind field, consistent with surface Ekman dynamics. At deeper depths, the current vectors generally rotate in a counter-clockwise direction, indicating the influence of the bottom Ekman layer. However, for winds toward 225° T and 270° T the currents rotate primarily clockwise with depth. In these cases the winds are directed off-shelf and the 5 m currents are directed nearly 90° to the right of the wind. We also note that currents at depth are more closely aligned along the model-derived SSH contours than are those near the surface. In aggregate, these observations are consistent with the flow field being in near-geostrophic balance and responding strongly to the interaction of the wind-driven Ekman flow with the convoluted Bering Sea coastline.

[60] The structure of the SSH field and its associated currents is highly sensitive to the wind direction. Northerly and northwesterly winds generate the strongest coastal divergence

(depressed SSHs over Chirikov Basin, Norton Sound and the central shelf), but the cross-isobath SSH gradient weakens considerably where the local coastline changes from a predominantly north-south orientation (between Norton Sound and Nunivak Island) to a more west-east orientation (in Kuskokwim Bay and Bristol Bay). The shelf response switches rather abruptly from divergent (northerly winds) to convergent (easterly winds) conditions.

[61] We note that the shelfbreak and outer shelf isobath orientations can be represented by a line extending from the northwest (Cape Navarin) to the southeast (Unimak Pass) and because the shelf flow field adjusts to northerly and easterly winds as described, we segregate all records into two modes based on the wind direction. The coastal convergence (i.e., downwelling) mode is associated with southeasterly winds and results in along-isobath currents directed toward Bering Strait. The coastal divergence (i.e., upwelling) mode is

Table 5. Comparison of the Cross-Correlation (r) Between Observed SSH Fluctuations and the BESTMAS Model SSH Hindcasts for Two Time Intervals^a

	N55	C55	S55	N40	S40	N25	C25
October–May	0.60	0.67	0.65	0.77	0.66	0.86	0.81
June–September	0.32	0.58	0.64	0.80	0.48	0.71	0.64

^aAll values are significant at the 95% level ($p < 0.05$).

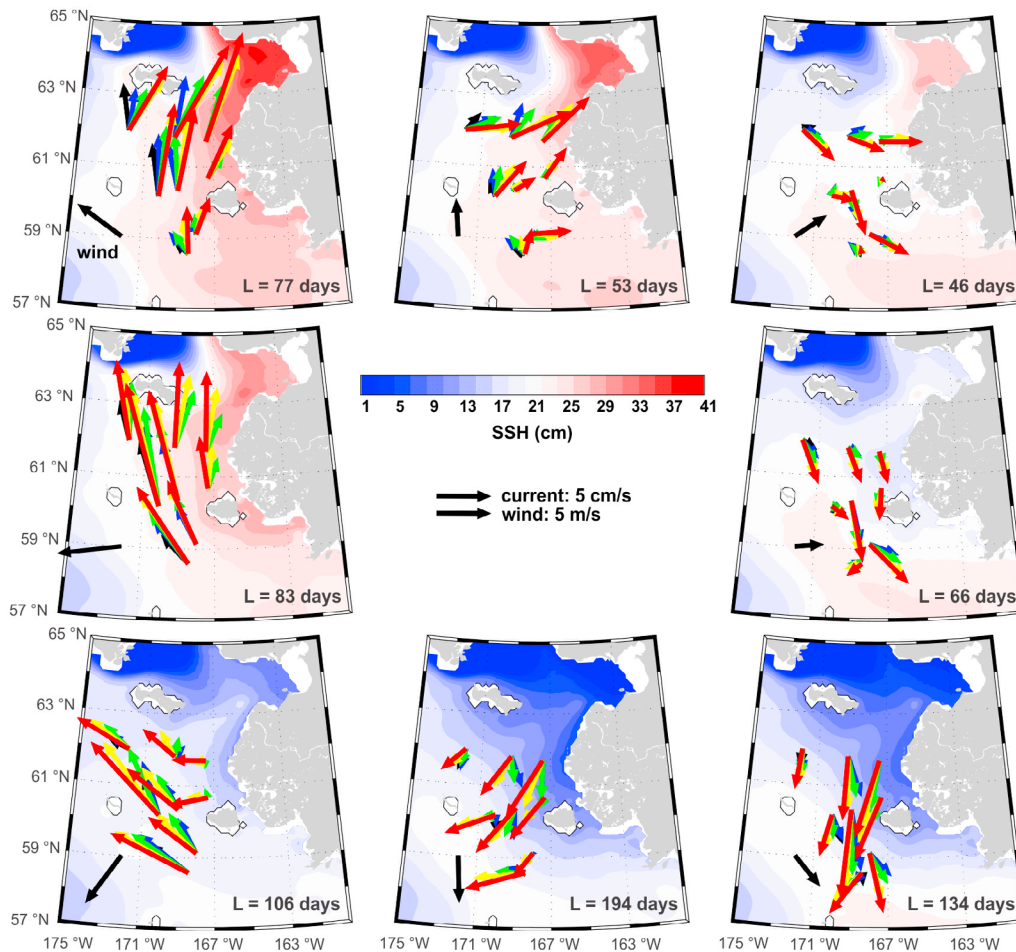


Figure 17. Composite oceanic response to various wind directions. Each panel is for a different set of wind directions (top center -22.5°T to $+22.5^{\circ}\text{T}$, etc.). The mean wind vector is the black vector emanating from 59°N , 172°W . Current vectors are color-coded based on depth: 5 m = red, 10 m = yellow, 20 m = green, 30 m = blue, 40 m = black. The BESTMAS SSH field is contoured at 2 cm increments between 1 cm (blue) and 41 cm (red) elevations and is clipped at levels beyond this, so that the entire dynamic range is not fully represented. The mean wind direction is over the 24-h period prior to the ocean current observation. L denotes the total time represented by each panel's average. A scale vector for both the wind and current is provided in the center.

associated with northwesterly winds and results in currents directed away from Bering Strait. Divergent conditions occurred 64% of the time over the course of our field program; convergent conditions occurred the remaining 36% of the time. Southeasterly wind, though less frequent during the measurement program, leads to stronger currents than northwesterly wind. The net effect of these competing circulation modes yields the highly variable but small mean currents that characterize the flow field of the eastern Bering shelf.

4. Discussion

[62] We have shown that currents over the central shelf are coherent over scales of ~ 200 km for most sub-inertial and sub-tidal frequencies and are moderately (but significantly) coherent with the local winds. Vertical coherence of the flow field is reduced during late spring and summer, coincident with reduced mean wind speeds and increased ocean stratification. Variations in SSH and the underlying current field are

sensitive to the direction of wind-forcing through the upwelling and downwelling responses of the Ekman transport, and the transition from upwelling to downwelling conditions occurs for winds directed approximately to the southwest [Danielson *et al.*, 2012].

[63] Our analysis suggests that the entire central Bering shelf circulation responds strongly to coastal convergence and divergence. Convergence is associated with enhanced northward flow resulting from coastal sea surface setup caused by onshore Ekman transport driven by southeasterly winds. Coastal divergence results from offshore Ekman transport driven by northwesterly winds. In general, southeasterly winds result in stronger flows, but northwesterly winds occur more often. Note, however, that our observations were made during two relatively cold years in the Bering Sea [Stabeno *et al.*, 2012]. We expect that Bering Sea warmer years will likely show a greater proportion of downwelling (i.e., southeasterly winds). Note also that the more energetic convergent response may at least in part be

due to the propagation direction of storms across the shelf. Cyclones typically approach the shelf from the southwest and so first impart northward momentum with their leading edge of southeasterly winds; the trailing edge (northwesterly winds) must first decelerate the northward flow before reversing the current direction. Not all high wind events, however, are associated with propagating low-pressure systems.

[64] Our synthesis of shelf behavior in fall and winter is consistent with the findings of *Danielson et al.* [2011], who used CTD survey data from the BASIS program to show that the freshwater content over the shelf is correlated with the October–May wind direction anomaly. Northerly winds promote offshore spreading of low-salinity coastal waters, whereas easterly winds promote northward along-shelf transport and presumably prevent offshore spreading of fresh water.

[65] We have also shown that the baroclinic pressure field reverses direction, from promoting southward flow in late winter to promoting northward flow in late summer. Because effects of heating and freezing are enhanced in shallow waters, warm summers increase the magnitude of the cross-shelf density difference and thus enhance northward transport, and cold winters with increased ice production and brine rejection also increased the magnitude of the (now reversed) cross-shelf density difference and enhance southward transport. Conversely, milder summers or winters lead to smaller cross-slope density differences, and thus weaker flow, so that the greater preponderance of southeasterly winds inhibits the offshore transport of dilute coastal waters. Thus, the baroclinic pressure gradients respond to the atmosphere's influence on both freezing and advective processes. (As a cautionary note, some atmospheric circulation patterns can result in warm Gulf of Alaska air being recirculated southward over the Bering Sea [*Rodionov et al.*, 2007], so that winds from the north are not always associated with enhanced ice production and brine rejection.) Although the baroclinic velocity is large enough to influence seasonal transports, it is not as important as the effect of the wind-driven convergences and divergences in setting up the shelf pressure field.

[66] Transport through Bering Strait increases in summer due to larger horizontal density gradients (presence of the Alaskan Coastal Current) and a reduction in northerly winds [*Roach et al.*, 1995; *Woodgate et al.*, 2005a, 2005b]. Surprisingly, the mean summer flow we observe over the shelf is not uniformly northward over the inner shelf, despite a cross-isobath baroclinic pressure gradient that promotes northward flow in summer. This suggests that much of the increased summer flow through Bering Strait comes from the Gulf of Anadyr, either directly through Anadyr Strait or from the eastward transport on the southern side of St. Lawrence Island, and/or from Alaskan Coastal Current waters inshore of our mooring array. Intriguingly, the BESTMAS model SSH field averaged over May–September, shows that a large majority of the SSH contours in the Gulf of Anadyr pass through Anadyr Strait, with only a small fraction directed eastward south of St. Lawrence Island before turning north in Shpanberg Strait. During October–April all the SSH contours pass directly through Anadyr Strait. Taken together, these findings suggest that waters from the central Bering shelf contributed relatively little to the Bering Strait throughflow over the course of our field years, with the possible exception

of summer waters immediately adjacent to the Alaskan coast, inshore of our moorings.

[67] Based on our observations reported here, together with those of *Schumacher et al.* [1983], *Danielson et al.* [2006] and *Danielson et al.* [2012], we propose that waters originating in the Gulf of Anadyr are a source of nutrient-rich waters to the central Bering shelf, particularly in winter. Indeed, the BESTMAS model SSH contours are consistent with our observations suggesting an advective pathway that extends eastward from the Gulf of Anadyr, passing south of St. Lawrence Island, and is then south- or southeastward toward Nunivak Island. This linkage occurs under northwesterly winds and is consonant with the mean October–April and May–September SSH fields (not shown). The model results of *Clement et al.* [2005] also show a southward flow tendency across the central shelf region in 1979, a year that their model indicated reduced northward transport through Bering Strait. Similarly, based on a two-month reversal of currents in Shpanberg Strait, *Muench et al.* [1988] schematically suggested a pathway for Chirikov Basin water (primarily of Anadyr origin) moving eastward north of St. Lawrence Island, and then southward through Shpanberg Strait. These various lines of evidence have important implications for biological production, since they suggest that the rich nutrient load in the Gulf of Anadyr can be brought onto the central shelf region at least as far south as Nunivak Island under sustained southeastward flow (e.g., a monthlong mean speed of 10 cm s^{-1}). Indeed, this nutrient pathway may at least in part explain the recent observation of elevated net community production over the central shelf [*Mathis et al.*, 2010].

[68] We further suggest that inter-annual variations in biological production over the central shelf may be linked to the long-term variability of the wind-driven southeastward circulation mode that we have described. We expect that winters with more northwesterly winds will increase the central shelf nutrient reservoir leading into spring and summer, while the fresh and nutrient-depleted coastal waters that normally reside over the central shelf will be carried south of Nunivak Island and farther offshore. Conversely, winters with more southeasterly winds will flush central shelf waters northward, some fraction possibly through Bering Strait, and increase on-shelf nutrient fluxes over the southern Bering shelf. Inter-annual variation in the preponderance and strength of northwesterly and southeasterly winds will therefore result in a variable supply of nutrients to large portions of the shelf, and possibly northward through Bering Strait. These ideas could be tested further with the data sets recently collected as part of the BEST-BSIERP program, along with analysis of new and existing numerical model integrations.

[69] The central shelf circulation alternates between the two described modes, resulting in a flow that is small in the mean but highly variable both spatially and temporally. Within this variable regime, we estimate residence time for the central shelf as follows. The distance from each mooring to its closest neighbor is 61–142 km, with a mean of 85 km. To cover these distances in one month would require a flow of $2.3\text{--}5.5 \text{ cm s}^{-1}$. Given that flows are largely coherent at low frequencies and within 200 km of each other (Figure 14), we assume a uniform flow field and integrate the raw velocity record at each mooring with respect to time. By progressively shifting the integration start by one observation time step

(30 min) through the velocity record, we compute the minimum time it would take a particle at 5 m depth to move 50 and 100 km from its initial position. We find that the probability distribution function is lognormal, with modal peaks centered near 6 and 12 days for the minimum time required to displace a particle in the upper water column 50 and 100 km, respectively. The durations lengthen to 14 and 34 days for currents at 30 m depth. For comparison, mean monthly vertically averaged velocities suggest typical monthly displacements of 30–90 km and maximum displacements of ~ 230 km. Taken together, these estimates suggest a mean residence time of many months, but two or three successive months of anomalous flow could largely flush the central shelf.

[70] It is unclear what changes over the central shelf mean for the northward transport through Bering Strait because *Danielson et al.* [2012] show that bi-directional exchange through both Anadyr and Shpanberg straits must be considered in the regional volume balance. Although winds over the central shelf are not coherent with those over Chirikov Basin, Bering Strait and the southern Chukchi Sea (Figure 8), the model results show that northwesterly and southeasterly winds over the mooring array are associated with SSH anomalies that extend to Chirikov Basin and Norton Sound (Figure 17). Comparison of observed monthly mean velocities at Bering Strait mooring MA3 to the fraction of time that wind at 60°N, 170°W blew from the southeast shows a weak but statistically significant relation ($r = 0.39$, $p = 0.002$) such that southeasterly winds are associated with northward transport anomalies in Bering Strait [*Aagaard and Schumacher*, 1985; *Woodgate et al.*, 2005a].

[71] Our results also suggest that some fraction of the Yukon River discharge may be advected westward across the central shelf under the southeastward circulation mode, first being brought southward past Nunivak Island and then westward with the offshore flow. Direct evidence is sparse, but tantalizing. Most notably, three of fifteen satellite-tracked drifters deployed near Nunivak Island in September 2002 headed west past Cape Navarin under the influence of generally northerly winds [*Danielson et al.*, 2006] (also see <http://www.ims.uaf.edu/drifters/>). More generally, the central Bering shelf may constitute a branch point between subarctic and arctic domains, with freshwater, heat, larvae, or contaminants on the inner shelf being transported either westward toward the deep basin or northward toward the Arctic, depending on the wind-driven circulation.

[72] Finally, retrospective analysis shows that the mean wind direction over the Bering shelf has changed in concert with recent climate and ecosystem regime shifts. One major change occurred during the mid-1970s North Pacific regime shift, coincident with a transition from more upwelling-favorable conditions to more downwelling-favorable [*Danielson et al.*, 2011]. Forecasts from global climate models suggest that climate warming may slightly deepen the Aleutian low and move it ~ 100 km northward within a few decades [*Salathé*, 2006]. Over the eastern Bering shelf, monthly mean sea level pressure (SLP) contours show little variability over 100 km scales, and so we would not expect a large change in wind direction over most of a year. September and October may be somewhat more sensitive to changes in the Aleutian low position, however, because the mean monthly isobars are oriented from NE to SW over the central shelf [*Pickart et al.*, 2009] and from NW to SE over the outer

southeastern shelf. For these months, a northward shift of the low would subject more of the eastern shelf to upwelling winds and increase the eastward flux of nutrients from the Gulf of Anadyr. Additional insights on this issue might be achieved from climate projection models by focusing on seasonally dependent changes in the position of the Aleutian low.

5. Conclusions

[73] We analyzed the data from an array of eight current meter moorings distributed over the central Bering Sea shelf between the 25 and 55-m isobaths, between 58.6°N and 62°N. We find that the along-shore currents are primarily geostrophic and vary in response to the wind-forced sea level gradients associated with coastal Ekman convergences and divergences. Cross-shore currents are also predominantly geostrophic, although surface stresses, bottom stresses, and local accelerations account up for up to 40% of the momentum balance, depending on season and location. Shelf waters near the mooring array alternately flow northward (under southeasterly winds) and southward (under northwesterly winds) in response to the winds and the sea level gradients they force, resulting in typical sub-tidal speeds of 3–12 cm s^{-1} , peak speeds of 65 cm s^{-1} , and vector means $< 5 \text{ cm s}^{-1}$.

[74] Density-controlled horizontal pressure gradients vary seasonally and promote northward flow in late summer and southward flow in late winter. However, the baroclinic pressure field is of secondary importance in the momentum balance compared to the wind-forced barotropic pressure field, and baroclinic forcing is likely muted following warmer winters and cooler summers.

[75] The two circulation modes associated with coastal convergence and divergence probably play a significant role in the freshwater, heat, and nutrient budgets of the central shelf. In particular, we suggest that waters from the Gulf of Anadyr (advected either eastward along the south side of St. Lawrence Island or southward from the Chirikov Basin) can provide inorganic nitrogen to the central shelf at least as far south as Nunivak Island. Wind direction controls the ocean circulation modes, and the transition between southward and northward currents occurs between winds directed southward and westward. One or two months of strongly anomalous flow conditions may be sufficient to replace large portions of the central shelf with nitrate-rich waters from the northwest.

[76] We observed northwesterly winds nearly twice as often as southeasterly winds, but this is probably not representative of all years. Extended re-orientation of the mean wind direction would likely result in systematic changes to the circulation and a shelf-wide reorganization of many physical, chemical and biological fluxes that impact regional heat and freshwater content, nutrient stocks, and primary production.

[77] **Acknowledgments.** We thank the many scientists and ships crews involved in the BEST, BSIERP and BASIS programs for help with mooring deployments, recoveries, and CTD and hydrographic sampling and processing. We thank L. Eisner for the BASIS program CTD data and Jackie Grebmeier and Lee Cooper for spring CTD data collected during and before the BEST program years. The network of moored observations described here is a partnership between the University of Alaska Fairbanks (UAF) and the University of Washington (UW). We thank D. Leech and J. Johnson for masterminding the moorings. This manuscript is listed as BEST-BSIERP publication 66. S. Danielson and T. Weingartner received

support from NSF grant ARC-0732771, K. Aagaard from NSF grant ARC-0732428, and J. Zhang and R. Woodgate from NSF grant ARC-0611967.

References

- Aagaard, K., and E. Carmack (1989), The role of sea ice and other fresh water in the Arctic circulation, *J. Geophys. Res.*, *94*, 14,485–14,498, doi:10.1029/JC094iC10p14485.
- Aagaard, K. A. T. R., and J. D. Schumacher (1985), On the wind-driven variability of the flow through Bering Strait, *J. Geophys. Res.*, *90*, 7213–7221, doi:10.1029/JC090iC04p07213.
- Aagaard, K., T. J. Weingartner, S. L. Danielson, R. A. Woodgate, G. C. Johnson, and T. E. Whitledge (2006), Some controls on flow and salinity in Bering Strait, *Geophys. Res. Lett.*, *33*, L19602, doi:10.1029/2006GL026612.
- Allen, J. S., and P. K. Kundu (1978), On the momentum, vorticity and mass balance on the Oregon Shelf, *J. Phys. Oceanogr.*, *8*, 13–27, doi:10.1175/1520-0485(1978)008<0013:OTMVAM>2.0.CO;2.
- Bond, N. A., J. E. Overland, and P. Turet (1994), Spatial and temporal characteristics of the wind forcing of the Bering Sea, *J. Clim.*, *7*(7), 1119–1130, doi:10.1175/1520-0442(1994)007<1139:SATCOT>2.0.CO;2.
- Brabets, T. P., B. Wang, and R. H. Meade (2000), Environmental and hydrological overview of the Yukon River Basin, Alaska and Canada, *U.S. Geol. Surv. Water Res. Invest. Rep.*, *99-4204*, 106 pp.
- Brink, K. H. (1998), Wind-driven currents over the continental shelf, in *The Sea*, vol. 10, *The Global Coastal Ocean*, edited by K. H. Brink and A. R. Robinson, pp. 3–20, John Wiley, New York.
- Brower, W. A., Jr., R. G. Baldwin, C. N. Williams Jr., J. L. Wise, and L. D. Leslie (Eds.) (1988), *Climate Atlas of the Outer Continental Shelf Waters and Coastal Regions of Alaska*, vol. 2, *Bering Sea*, Natl. Clim. Data Cent., Asheville, N. C.
- Cherniawsky, J. Y., W. R. Crawford, O. P. Nikitin, and E. C. Carmack (2005), Bering Strait transports from satellite altimetry, *J. Mar. Res.*, *63*(5), 887–900, doi:10.1357/002224005774464201.
- Clement, J. L., W. Maslowski, L. W. Cooper, J. M. Grebeiner, and W. Walczowski (2005), Ocean circulation and exchanges through the northern Bering Sea: 1979–2001, *Deep Sea Res., Part II*, *52*, 3509–3540, doi:10.1016/j.dsr2.2005.09.010.
- Clement Kinney, J., W. Maslowski, and S. Okkonen (2009), On the processes controlling shelf-basin exchange and outer shelf dynamics in the Bering Sea, *Deep Sea Res., Part II*, *56*, 1351–1362, doi:10.1016/j.dsr2.2008.10.023.
- Coachman, L. K. (1986), Circulation, water masses, and fluxes on the southeastern Bering Sea shelf, *Cont. Shelf Res.*, *5*, 23–108, doi:10.1016/0278-4343(86)90011-7.
- Coachman, L. K. (1993), On the flow field in the Chirikov Basin, *Cont. Shelf Res.*, *13*, 481–508, doi:10.1016/0278-4343(93)90092-C.
- Coachman, L. K., and K. Aagaard (1988), Transports through Bering Strait: Annual and interannual variability, *J. Geophys. Res.*, *93*(C12), 15,535–15,539, doi:10.1029/JC093iC12p15535.
- Coachman, L. K., K. Aagaard, and R. B. Tripp (1975), *Bering Strait: The Regional Physical Oceanography*, Univ. of Wash. Press, Seattle.
- Danielson, S., and Z. Kowalik (2005), Tidal currents in the St. Lawrence Island region, *J. Geophys. Res.*, *110*, C10004, doi:10.1029/2004JC002463.
- Danielson, S., K. Aagaard, T. Weingartner, S. Martin, P. Winsor, G. Gawarkiewicz, and D. Quadfasel (2006), The St. Lawrence polynya and the Bering shelf circulation: New observations that test the models, *J. Geophys. Res.*, *111*, C09023, doi:10.1029/2005JC003268.
- Danielson, S., L. Eisner, T. Weingartner, and K. Aagaard (2011), Thermal and haline variability over the central Bering Sea shelf: Seasonal and interannual perspectives, *Cont. Shelf Res.*, *31*, 539–554, doi:10.1016/j.csr.2010.12.010.
- Danielson, S., K. Hedstrom, K. Aagaard, T. Weingartner, and E. Curchitser (2012), Wind-induced reorganization of the Bering shelf circulation, *Geophys. Res. Lett.*, *39*, L08601, doi:10.1029/2012GL051231.
- Drucker, R., S. Martin, and R. Moritz (2003), Observations of ice thickness and frazil ice in the St. Lawrence Island polynya from satellite imagery, upward looking sonar, and salinity/temperature moorings, *J. Geophys. Res.*, *108*(C5), 3149, doi:10.1029/2001JC001213.
- Emory, W. J., and R. E. Thompson (2001), *Data Analysis Methods in Physical Oceanography*, 2nd ed., Elsevier, San Diego, Calif.
- Favorite, F. (1974), Flow into the Bering Sea through Aleutian island passes, in *Oceanography of the Bering Sea, Occas. Publ. 2*, edited by D. W. Hood and E. J. Kelley, pp. 3–37, Inst. of Mar. Sci., Univ. of Alaska Fairbanks, Fairbanks.
- Foreman, M. G. G. (1978), Manual for tidal currents analysis and prediction, *Pac. Mar. Sci. Rep.* 78-6, 57 pp., Inst. of Ocean Sci., Sidney, B. C., Canada.
- Hibler, W. D., III (1980), Modeling a variable thickness sea ice cover, *Mon. Weather Rev.*, *108*, 1943–1973, doi:10.1175/1520-0493(1980)108<1943:MAVTSI>2.0.CO;2.
- Hill, A. E. (1996), Spin-down and the dynamics of dense pool gyres in shallow seas, *J. Mar. Res.*, *54*, 471–486, doi:10.1357/0022240963213538.
- Jackson, J. M., E. C. Carmack, F. A. McLaughlin, S. E. Allen, and R. G. Ingram (2010), Identification, characterization, and change of the near-surface temperature maximum in the Canada Basin, 1993–2008, *J. Geophys. Res.*, *115*, C05021, doi:10.1029/2009JC005265.
- Johnson, G. C., P. J. Stabeno, and S. C. Riser (2004), The Bering Slope Current system revisited, *J. Phys. Oceanogr.*, *34*, 384–398, doi:10.1175/1520-0485(2004)034<0384:TBSCSR>2.0.CO;2.
- Kachel, N. B., G. L. Hunt Jr., S. A. Salo, J. D. Schumacher, P. J. Stabeno, and T. E. Whitledge (2002), Characteristics and variability of the inner front of the southeastern Bering Sea, *Deep Sea Res., Part II*, *49*, 5889–5909, doi:10.1016/S0967-0645(02)00324-7.
- Kalnay E., et al. (1996), The NCEP/NCAR 40-year reanalysis project, *Bull. Am. Meteorol. Soc.*, *77*, 437–471, doi:10.1175/1520-0477(1996)077<0437:TNYRP>2.0.CO;2.
- Kinder, T. H., and J. D. Schumacher (1981), Hydrographic structure over the continental shelf of the southeastern Bering Sea, in *The Eastern Bering Sea Shelf, Oceanography and Resources*, vol. 1, edited by D. W. Hood and J. A. Calder, pp. 31–52, Univ. of Wash. Press, Seattle.
- Kinder, T. J., D. C. Chapman, and J. A. Whitehead (1986), Westward intensification of the mean circulation on the Bering Sea shelf, *J. Phys. Oceanogr.*, *16*, 1217–1229, doi:10.1175/1520-0485(1986)016<1217:WIOTMC>2.0.CO;2.
- Kowalik, Z. (1999), Bering Sea tides, in *Dynamics of The Bering Sea: A Summary of Physical, Chemical and Biological Characteristics, and a Synopsis of Research on the Bering Sea*, edited by T. R. Loughlin and K. Ohtani, pp. 93–127, Univ. of Alaska Sea Grant, Fairbanks.
- Ladd, C., and N. Bond (2002), Evaluation of the NCEP/NCAR reanalysis in the NE Pacific and the Bering Sea, *J. Geophys. Res.*, *107*(C10), 3158, doi:10.1029/2001JC001157.
- Ladd, C., and P. J. Stabeno (2012), Stratification on the eastern Bering Sea shelf, revisited, *Deep Sea Res., Part II*, *65–70*, 72–83, doi:10.1016/j.dsr2.2012.02.009.
- Large, W. G., and S. Pond (1981), Open ocean momentum flux measurements in moderate to strong winds, *J. Phys. Oceanogr.*, *11*, 324–336, doi:10.1175/1520-0485(1981)011<0324:OOMFMI>2.0.CO;2.
- Lentz, S. J., and C. D. Winant (1986), Subinertial currents on the southern California shelf, *J. Phys. Oceanogr.*, *16*, 1737–1750, doi:10.1175/1520-0485(1986)016<1737:SCOTSC>2.0.CO;2.
- Mathis, J. T., J. N. Cross, N. R. Bates, S. B. Moran, M. W. Lomas, P. J. Stabeno, and C. W. Mordy (2010), Seasonal distribution of dissolved inorganic carbon and net community production on the Bering Sea shelf, *Biogeosciences*, *7*, 1769–1787, doi:10.5194/bg-7-1769-2010.
- McNutt, L. (1981), Ice conditions in the eastern Bering Sea from NOAA and LANDSAT imagery: Winter conditions 1974, 1976, 1977, 1979, *NOAA Tech. Memo., ERL PMEL-24*, 179 pp.
- McPhee, M. G. (1980), An analysis of pack ice drift in summer, in *Sea Ice Processes and Models*, edited by R. S. Pritchard, pp. 62–75, Univ. of Wash. Press, Seattle.
- Mesinger, F., et al. (2006), North American regional re-analysis, *Bull. Am. Meteorol. Soc.*, *87*, 343–360, doi:10.1175/BAMS-87-3-343.
- Mofjeld, H. O. (1984), Recent observations of tides and tidal currents from the northeastern Bering Sea shelf, *NOAA Tech. Memo., ERL PMEL-57*, 36 pp.
- Muench, R. D., and K. Ahlnas (1976), Ice movement and distribution in the Bering Sea from March to June 1974, *J. Geophys. Res.*, *81*(24), 4467–4476, doi:10.1029/JC081i024p04467.
- Muench, R. D., J. D. Schumacher, and S. A. Salo (1988), Winter currents and hydrographic conditions on the northern central Bering Sea shelf, *J. Geophys. Res.*, *93*(C1), 516–526, doi:10.1029/JC093iC01p00516.
- Mull, J. M. (2008), QuikSCAT measurements of the wind field over the Bering and Chukchi Seas, MS thesis, Univ. of Alaska Fairbanks, Fairbanks.
- Mundy, P. R., and D. F. Evenson (2011), Environmental controls of phenology of high-latitude Chinook salmon populations of the Yukon River, North America, with application to fishery management, *J. Mar. Sci.*, *68*, 1155–1164.
- Niebauer, H. J., N. A. Bond, L. P. Yakunin, and V. V. Plotnikov (1999), An update on the climatology and sea ice of the Bering Sea, in *Dynamics of the Bering Sea: A Summary of Physical, Chemical and Biological Characteristics, and a Synopsis of Research on the Bering Sea*, edited by T. R. Loughlin and K. Ohtani, pp. 29–59, Univ. of Alaska Sea Grant, Fairbanks.
- Okkonen, S. (1993), Observations of topographic planetary waves in the Bering Slope Current using Geosat altimeter, *J. Geophys. Res.*, *98*(C12), 22,603–22,613, doi:10.1029/93JC02344.
- Orensanz, J., B. Ernst, D. Armstrong, P. Stabeno, and P. Livingston (2004), Contraction of the geographic range of distribution of snow crab

- (*Chionoecetes opilio*) in the eastern Bering Sea: An environmental ratchet?, *CCOFI Rep.*, 45, 65–79.
- Overland, J. E., and C. H. Pease (1982), Cyclone climatology of the Bering Sea and its relation to sea ice extent, *Mon. Weather Rev.*, 110, 5–13, doi:10.1175/1520-0493(1982)110<0005:CCOTBS>2.0.CO;2.
- Overland, J. E., and A. T. Roach (1987), Northward flow in the Bering and Chukchi Seas, *J. Geophys. Res.*, 92, 7097–7105, doi:10.1029/JC092iC07p07097.
- Overland, J. E., M. C. Spillane, H. Y. Hurlburt, and A. J. Wallcraft (1994), A numerical study of the circulation of the Bering Sea basin and exchange with the north Pacific Ocean, *J. Phys. Oceanogr.*, 24, 736–758, doi:10.1175/1520-0485(1994)024<0736:ANSOTC>2.0.CO;2.
- Pawlowicz, R., B. Beardsley, and S. Lentz (2002), Classical tidal harmonic analysis including error estimates in MATLAB using T_TIDE, *Comput. Geosci.*, 28, 929–937, doi:10.1016/S0098-3004(02)00013-4.
- Pearson, C. A., H. O. Mofjeld, and R. B. Tripp (1981), Tides of the eastern Bering Sea Shelf, in *The Eastern Bering Sea Shelf: Oceanography and Resources*, vol. 1, edited by D. W. Hood, and J. A. Calder, pp. 111–130, Univ. of Wash. Press, Seattle.
- Pease, C. H. (1980), Eastern Bering Sea ice processes, *Mon. Weather Rev.*, 108, 2015–2023, doi:10.1175/1520-0493(1980)108<2015:EBSIP>2.0.CO;2.
- Pease, C. H. (1981), Eastern Bering Sea ice dynamics and thermodynamics, in *The Eastern Bering Sea Shelf: Oceanography and Resources*, vol. 1, edited by D. W. Hood and J. A. Calder, pp. 213–222, Univ. of Wash. Press, Seattle.
- Pickart, R. S., G. W. K. Moore, A. M. Macdonald, I. A. Renfrew, J. E. Walsh, and W. S. Kessler (2009), Seasonal evolution of Aleutian low-pressure systems: Implications for the North Pacific sub-polar circulation, *J. Phys. Oceanogr.*, 39, 1317–1339, doi:10.1175/2008JPO3891.1.
- Reed, R. K., and P. J. Stabeno (2002), Surface heat fluxes and subsurface heat content at a site over the southeastern Bering Sea shelf, May–June 1996, *Deep Sea Res., Part II*, 49, 5911–5917, doi:10.1016/S0967-0645(02)00325-9.
- Reynolds, R. W., and T. M. Smith (1994), Improved global sea surface temperature analyses using optimum interpolation, *J. Clim.*, 7, 929–948, doi:10.1175/1520-0442(1994)007<0929:IGSSTA>2.0.CO;2.
- Reynolds, R. W., N. A. Rayner, T. M. Smith, D. C. Stokes, and W. Wang (2002), An improved in situ and satellite SST analysis for climate, *J. Clim.*, 15, 1609–1625, doi:10.1175/1520-0442(2002)015<1609:AII-SAS>2.0.CO;2.
- Roach, A. T., K. Aagaard, C. H. Pease, S. A. Salo, T. Weingartner, V. Pavlov, and M. Kulakov (1995), Direct measurements of transport and water properties through Bering Strait, *J. Geophys. Res.*, 100, 18,443–18,457, doi:10.1029/95JC01673.
- Roden, G. I. (1995), Aleutian Basin of the Bering Sea: Thermohaline, oxygen, nutrient, and current structure in July 1993, *J. Geophys. Res.*, 100(C7), 13,539–13,554, doi:10.1029/95JC01291.
- Rodionov, S. N., N. A. Bond, and J. E. Overland (2007), The Aleutian low, storm tracks, and winter climate variability in the Bering Sea, *Deep Sea Res., Part II*, 54(23–26), 2560–2577, doi:10.1016/j.dsr2.2007.08.002.
- Royer, T. C., and W. J. Emery (1984), Circulation in the Bering Sea, 1982–83, based on satellite-tracked drifter observations, *J. Phys. Oceanogr.*, 14, 1914–1920, doi:10.1175/1520-0485(1984)014<1914:CITBS>2.0.CO;2.
- Salathé, E. P., Jr. (2006), Influences of a shift in North Pacific storm tracks on western North American precipitation under global warming, *Geophys. Res. Lett.*, 33, L19820, doi:10.1029/2006GL026882.
- Sambrotto, R. N., H. J. Niebauer, J. J. Goering, and R. L. Iverson (1986), Relationships among vertical mixing, nitrate uptake and phytoplankton growth during the spring bloom in the southeast Bering Sea middle shelf, *Cont. Shelf Res.*, 5, 161–198, doi:10.1016/0278-4343(86)90014-2.
- Schumacher, J. D., and T. H. Kinder (1983), Low-frequency current regimes over the Bering Sea shelf, *J. Phys. Oceanogr.*, 13, 607–623, doi:10.1175/1520-0485(1983)013<0607:LFCROT>2.0.CO;2.
- Schumacher, J. D., and R. K. Reed (1992), Characteristics of currents over the continental slope of the eastern Bering Sea, *J. Geophys. Res.*, 97(C6), 9423–9433, doi:10.1029/92JC00512.
- Schumacher, J. D., C. A. Pearson, and J. E. Overland (1982), On exchange of water between the Gulf of Alaska and the Bering Sea through Unimak Pass, *J. Geophys. Res.*, 87, 5785–5795, doi:10.1029/JC087iC08p05785.
- Schumacher, J., K. Aagaard, C. Pease, and R. Tripp (1983), Effects of a shelf polynya on flow and water properties in the northern Bering Sea, *J. Geophys. Res.*, 88(C5), 2723–2732, doi:10.1029/JC088iC05p02723.
- Smith, R. D., J. K. Dukowicz, and R. C. Malone (1992), Parallel ocean general circulation modeling, *Physica D*, 60, 38–61, doi:10.1016/0167-2789(92)90225-C.
- Spaulding, M., T. Isaji, D. Mendelsohn, and A. C. Turner (1987), Numerical simulation of wind-driven flow through the Bering Strait, *J. Phys. Oceanogr.*, 17, 1799–1816, doi:10.1175/1520-0485(1987)017<1799:NSOWDF>2.0.CO;2.
- Stabeno, P. J., N. A. Bond, N. B. Kachel, S. A. Salo, and J. D. Schumacher (2001), On the temporal variability of the physical environment over the southeastern Bering Sea, *Fish. Oceanogr.*, 10(1), 81–98, doi:10.1046/j.1365-2419.2001.00157.x.
- Stabeno, P. J., N. B. Kachel, M. Sullivan, and T. E. Whitedge (2002a), Variability of physical and chemical characteristics along the 70-m isobath of the southeast Bering Sea, *Deep Sea Res., Part II*, 49(26), 5931–5943, doi:10.1016/S0967-0645(02)00327-2.
- Stabeno, P. J., R. K. Reed, and J. M. Napp (2002b), Transport through Unimak Pass, Alaska, *Deep Sea Res., Part II*, 49(26), 5919–5930, doi:10.1016/S0967-0645(02)00326-0.
- Stabeno, P. J., C. Ladd, and R. K. Reed (2009), Observations of the Aleutian north slope current, Bering Sea 1996–2001, *J. Geophys. Res.*, 114, C05015, doi:10.1029/2007JC004705.
- Stabeno, P. J., J. M. Napp, C. W. Mordy, and T. E. Whitedge (2010), Factors influencing physical structure and lower trophic levels of the eastern Bering Sea shelf in 2005: Sea ice, tides and winds, *Prog. Oceanogr.*, 85, 180–196, doi:10.1016/j.pocan.2010.02.010.
- Stabeno, P., N. Kachel, S. Moore, J. Napp, M. Sigler, A. Yamaguchi, and A. Zerbini (2012), Comparison of warm and cold years on the southeastern Bering Sea shelf, *Deep Sea Res., Part II*, 65–70, 31–45, doi:10.1016/j.dsr2.2012.02.020.
- Stigebrandt, A. (1984), The North Pacific: A global-scale estuary, *J. Phys. Oceanogr.*, 14, 464–470, doi:10.1175/1520-0485(1984)014<0464:TNPAGS>2.0.CO;2.
- Takenouti, A. Y., and K. Ohtani (1974), Currents and water masses in the Bering Sea: A review of Japanese work, in *Oceanography of the Bering Sea, Occas. Publ. 2*, edited by D. W. Hood and E. J. Kelley, pp. 39–58, Inst. of Mar. Sci., Univ. of Alaska Fairbanks, Fairbanks.
- U.N. Educational, Scientific and Cultural Organization (1981), The Practical Salinity Scale 1978 and the International Equation of State of Seawater 1980, *Tech. Pap. Mar. Sci.*, 36, Paris.
- Weingartner, T. J., S. L. Danielson, and T. C. Royer (2005), Fresh water variability and predictability in the Alaska Coastal Current, *Deep Sea Res., Part II*, 52, 169–191, doi:10.1016/j.dsr2.2004.09.030.
- Wespestad, V. G., L. W. Fritz, W. J. Ingraham, and B. A. Megrey (2000), On relationships between cannibalism, climate variability, physical transport, and recruitment success of Bering Sea walleye pollock (*Theragra chalcogramma*), *J. Mar. Sci.*, 57, 268–274.
- Whitedge, T. E., W. S. Reeburgh, and J. J. Walsh (1986), Seasonal inorganic nitrogen distribution and dynamics in the southeastern Bering Sea, *Cont. Shelf Res.*, 5, 109–132, doi:10.1016/0278-4343(86)90012-9.
- Wilderbuer, T. K., A. B. Hollowed, W. J. Ingraham, P. D. Spencer, M. E. Conners, N. A. Bond, and G. Walters (2002), Flatfish recruitment response to decadal climate variability and ocean conditions in the eastern Bering Sea, *Prog. Oceanogr.*, 55, 235–247, doi:10.1016/S0079-6611(02)00081-2.
- Wilson, J. G., and J. E. Overland (1986), Meteorology, in *The Gulf of Alaska: Physical Environment and Biological Resources*, edited by D. W. Hood and S. T. Zimmerman, pp. 31–54, Alaska Off., Ocean Assess. Div., NOAA, Washington, D. C.
- Woodgate, R. A., K. Aagaard, and T. J. Weingartner (2005a), Monthly temperature, salinity, and transport variability of the Bering Strait through flow, *Geophys. Res. Lett.*, 32, L04601, doi:10.1029/2004GL021880.
- Woodgate, R. A., K. Aagaard, and T. J. Weingartner (2005b), A year in the physical oceanography of the Chukchi Sea: Moored measurements from autumn 1990–1991, *Deep Sea Res., Part II*, 52(24–26), 3116–3149, doi:10.1016/j.dsr2.2005.10.016.
- Woodgate, R. A., T. J. Weingartner, and R. Lindsay (2010), The 2007 Bering Strait oceanic heat flux and anomalous Arctic sea-ice retreat, *Geophys. Res. Lett.*, 37, L01602, doi:10.1029/2009GL041621.
- Zhang, J., and D. A. Rothrock (2001), A thickness and enthalpy distribution sea-ice model, *J. Phys. Oceanogr.*, 31, 2986–3001, doi:10.1175/1520-0485(2001)031<2986:ATAEDS>2.0.CO;2.
- Zhang, J., and D. A. Rothrock (2003), Modeling global sea ice with a thickness and enthalpy distribution model in generalized curvilinear coordinates, *Mon. Weather Rev.*, 131, 845–861, doi:10.1175/1520-0493(2003)131<0845:MGSIIWA>2.0.CO;2.
- Zhang, J., R. A. Woodgate, and R. Moritz (2010), Sea ice response to atmospheric and oceanic forcing in the Bering Sea, *J. Phys. Oceanogr.*, 40, 1729–1747, doi:10.1175/2010JPO4323.1.
- Zhang, J., R. Woodgate, and S. Mangiameli (2012), Towards seasonal prediction of the distribution and extent of cold bottom waters on the Bering Sea shelf, *Deep Sea Res., Part II*, 65–70, 58–71, doi:10.1016/j.dsr2.2012.02.023.